

Technical report

# Satellite altimeter models for surface wind speed developed using ocean satellite crossovers

J. Gourrion<sup>1</sup>, D. Vandemark<sup>2</sup>, S. Bailey<sup>2</sup>, B. Chapron<sup>1</sup>

<sup>1</sup> Ifremer, DRO/OS, Plouzané, FRANCE

<sup>2</sup> NASA/Goddard Space Flight Center, Wallops Island, Virginia, USA

May 17<sup>th</sup>, 2000

Report No. : IFREMER-DROOS-2000-02

## Abstract

A large global compilation of altimeter and scatterometer satellite crossover samples is used to address altimeter wind speed inversion. The emphasis here is altimeter wind error due to sea state impacts. Numerous past studies have suggested that long-scale gravity waves, which do not adjust to wind as quickly as the short gravity-capillary waves, have a measurable influence on interpretation of altimeter returns in terms of wind speed. This hypothesis is affirmed here. TOPEX altimeter operational wind speed estimates are compared with NSCAT-derived surface winds to show a clear correlation between altimeter wind error and the TOPEX-derived significant wave height (SWH) estimate. This observation holds for both the C and Ku-band frequencies of TOPEX. Candidate empirical algorithms using both altimeter backscatter and wave height estimates are then developed to remove the observed average significant wave height signature from altimeter-derived wind speeds. These algorithms are developed for global application and validated using numerous independent sources to confirm that slight but statistically-significant global error reductions (e.g. 10-15 % reduction in rms error) are obtained. An algorithm for potential operational use is proposed and detailed.

Our study indicates that inclusion of the altimeter's wave height parameter provides limited additional improvement to the point-to-point accuracy of the wind speed estimates. This finding is consistent with the understanding that SWH is a crude descriptor for the complexities of actual gravity wave conditions where some mix of sea and swell is nearly always in evidence.

The suite of altimeter algorithms (C and Ku-band) presented here may aid global climate studies and refinement of other satellite sensor or numerical model wind estimates. They should also serve to improve our present understanding of the electromagnetic range bias phenomenon that corrupts altimetric sea surface topography measurements.

# 1 Introduction

Many empirical studies have been directed at developing an improved satellite altimeter ocean wind speed algorithm using differing numerical approaches and data sets (e.g. Brown et al., 1981; Dobson et al., 1987; Chelton and McCabe, 1985; Witter and Chelton, 1991; Glazman and Greysukh, 1993; Young, 1993; Lefevre et al., 1994; Freilich and Challenor, 1994 ). The global altimeter ocean wind product is mostly limited to validation and climatological usage (e.g. Young, 1999) because the altimeter's nadir-pointing geometry only permits estimates of surface wind speed along a narrow (  $\sim 2$  km) swath without wind direction information. However, accurate wind speed estimates from the altimeter are important for their uses mentioned above and because altimeter wind speed is used in a point-by-point correction of the sensor's estimate of mean sea surface level via the electromagnetic bias algorithm. Freilich and Challenor (1994) and Glazman and Greysukh (1993) expand on these points and both studies suggest that objective criterion for evaluating algorithm improvement should include the minimization of wind speed biases and root-mean-square error, removal of non-wind geophysical impacts such as sea state, and functional continuity (finite first derivative) such that the wind speed histogram is not distorted.

At present, the operational altimeter wind speed algorithm for the TOPEX/Poseidon satellite altimeters is derived from interpolation over the look up table known as the modified Chelton-Wentz algorithm ("MCW" , Witter and Chelton, 1991 ). This algorithm directly maps measured altimeter backscatter at Ku-band to near-surface wind speed. The overall bias,  $\langle e \rangle$ , for this algorithm is suggested to be  $+0.48$  m/s (  $e = U_{altim.} - U_{insitu}$  ) and the root-mean-square (rms) error lies between 1.5 and 2.0 m/s (e.g. Witter and Chelton, 1991; Gower, 1996; Freilich and Challenor, 1994; Wu, 1999 ). Numerous studies have suggested that the form for this single parameter algorithm could be improved upon (e.g. Freilich and Challenor, 1994 ). However, the limited amount of samples, and thus certainty, provided by altimeter/buoy validation sets combine with a small level of improvement to leave MCW as the current choice for new altimeters such as the GEOSAT Follow-On (GFO) and JASON-1.

An issue that has remained of interest within altimeter wind model studies is the ability to detect and correct for sensor wind speed errors associated with ocean waves that are not closely coupled to the local wind field. An obvious attraction in these efforts is that the altimeter provides an accurate measure of the ocean's significant wave height, SWH , along with every radar cross section estimate. Physically and observationally - it is well known that SWH is at best a partial indicator of the actual wave conditions that would be better described by, for example, a measurement of the directional wave height spectrum. Still, evidence for a sea state effect on altimeter-derived wind has been addressed in several studies (Monaldo and Dobson, 1989; Glazman and Pilorz, 1990; Glazman and Greysukh, 1993; Lefevre et al., 1994; Freilich and Challenor, 1994; Hwang, 1998 ) that make use of SWH estimates. Reported results range from substantial impacts to no impact (cf. Wu, 1999 ). Several wind speed algorithms that use both backscatter and wave height have been suggested (e.g. Lefevre et al., 1994; Glazman and Greysukh, 1993; Bentamy et al., 1999 ). Most studies appear to agree that the effect is clearly of second order and that SWH ( or pseudo wave age as in Glazman and Greysukh, 1993) serves as a limited proxy for removing non-wind or sea state impacts from the altimeter wind speed estimate.

The use of the C-band channel to enhance wind speed accuracy is another relevant issue for dual-frequency altimeters such as TOPEX and the upcoming JASON-1 (e.g. Chapron et al., 1995; Elfouhaily et al., 1997). These studies have shown that the small difference between the Ku and C-band backscatter is well-correlated with the local surface wind, particularly for moderate to high wind speeds. An inherently low signal-to-noise ratio and the importance of precise sensor calibration have made the use of this measurement difficult to date. The present study does not address this combination of the two channels. Results from that continuing effort will be reported at a later date. Rather, we will document here the basic relationship between TOPEX's C-band radar cross section  $\sigma_C^o$  and the near-surface wind speed.

This study provides several new mono-frequency (both at Ku- and C-band) altimeter wind speed algorithms that attempt to globally correct for sea state impacts using altimeter-derived SWH estimates. Motivation for the study comes from the collocation of a very large number of TOPEX altimeter observations with global surface wind estimates made using the NASA scatterometer (NSCAT) in 1996 and 1997. The volume, global coverage, and fidelity of this data lead to a much clearer picture of the average impact of sea state upon altimeter backscatter at different wind speeds and for different ocean basins. A long wave signature is measureable though our algorithm developments indicate that SWH is indeed of limited value in improving point-to-point accuracy of wind speed estimates. Proposed wind speed algorithms are devised using the help of neural network solutions to map between the altimeter and scatterometer estimates.

Our report is organized as follows. First the data sets assembled for the development and validation of the wind speed models will be provided. Next we discuss the characteristics of the colocated TOPEX and NSCAT data set in terms of wind speed errors and the indication of sea state impacts. The following section provides the neural network methodologies and resulting solutions for mapping the Ku-band backscatter and significant wave height into a near surface wind speed estimate. This section also demonstrates that the forward and inverse mapping of these data are not equivalent. In section four we attempt to objectively compare the accuracy of these new wind speed algorithms with numerous past algorithms. These routines are applied to a variety of independent validation data sets. Our recommendation for a new operational Ku-band algorithm is given with along with the improvements expected. The range of validity for this algorithm is 0-20 m/s. The same data and procedures used in the Ku-band developments are then applied to the C-band data set to document the wind response of TOPEX's C-band altimeter backscatter measurements. A discussion section will attempt to summarize the limits of and promise for future altimeter wind speed studies based on these investigations.

## 2 Observations

### 2.1 Data description

Previous studies have addressed altimeter wind speed models by examining altimeter measurements colocated with buoy or model data, or by some statistical means using other nearby satellite or global wind model information (cf. Witter and Chelton, 1991 ; Freilich and Challenor, 1994 ). This study follows the collocation approach and we make use of the unprecedented ability to combine TOPEX satellite altimeter measurements with those made at the same time and place by the NASA scatterometer. The resulting crossover data set is very large and forms the basis for our algorithm development and initial validation. The reasoning for this choice and details related to the production of this combined data are given below.

We also describe several other combined data sets that will be used for subsequent altimeter wind speed model validations and intercomparisons. These data sets represent similar crossover compilations using other global satellite reference scatterometer winds (ERS and SeaWinds), surface model winds (ECMWF) and buoy winds. We include data from the ERS and Geosat radar altimeters. The varied data sets offer the opportunity to assess algorithm stability with respect to bias, rms errors and removal of wave height impacts. Moreover, inherent data set differences provide some insight into issues such as intercomparison noise.

#### 2.1.1 Combining TOPEX and NSCAT

A choice must usually be made in wind speed algorithm developments between evaluating a small amount of measurements collected over fixed-location (often near to shore) ocean buoys and methods that utilize global wind statistics as the basis for tailoring the algorithm. A new option is becoming apparent in that numerous ocean observing satellites are now often in orbit at the same time. Many of these satellites share wind observing attributes that can be exploited when their respective ocean footprints cross. The primary assumption in our study is that the high quality surface wind observations gathered by the NSCAT can be used as surface truth for those points where near-simultaneous TOPEX and NSCAT observations occurred. The colocated data set has the attributes of very high spatial and temporal correlation, large data population and global coverage.

Moreover, a specific benefit for this case is the availability of a special high resolution scatterometer product produced by S. Dunbar at the Jet Propulsion Laboratory. It is well-known that wind estimate results can differ depending on intercomparison product resolutions and spatial and temporal separation, a fact that is already well documented from an altimeter wind comparison standpoint (e.g. Monaldo et al., 1989; Gower, 1996; Hwang, 1998; Freilich and Dunbar, 1993 ). A study objective is to discern sea state impacts on altimeter wind. Past studies and the known characteristics of wind wave growth suggest such an impact may occur or be apparent over fairly small spatial scales of order 10-100 km. For instance, the most common fetch for a wind sea on the ocean is about 70 km (e.g. Tournadre and Blanquet, 1994 ). Not surprisingly, the horizontal spatial extent

of atmospheric mesoscale activities falls into this range as well. To probe the long wave impacts on the satellite winds we then wish to obtain the finest scale intercomparison data set as possible.

The NSCAT wind speed data used for our study comes from the High Resolution Merged Geophysical Data Product ("HR-MGDR", Dunbar, 1997 ). The document of Dunbar (1997) describes the basic configuration of the six antenna satellite and the method for wind speed inversion from the radar backscatter measurements. Of particular note here is that the surface resolution is 25 km x 25 km for each wind estimate, a so-called wind vector cell. To keep sampling errors to a minimum we desire equal sensor surface coverage. Thus, this high resolution NSCAT product is also beneficial for this purpose as the TOPEX wind resolution cell is relatively miniscule - of the order of 2 x 6 km. Larger footprint ( $50\text{km}^2$ ) products such as from SSM/I, NSCAT, or ERS1-2 would encompass an area four times larger than this HGDR product. The algorithm used to derive wind speed for our data set was the NSCAT-1 (Wentz and Smith, 1999 ). A new algorithm, NSCAT-2 is now in existence. Its inclusion into our data set would not be straightforward but the changes between NSCAT-1 and 2 have been evaluated and found to be small in their wind speed impacts for the range of data (1-20 m/s) of interest here. Our independent validations of section four suggest this is the case. There we include evaluation of results against a colocation of TOPEX with NASA's SeaWinds scatterometer that uses the NSCAT-2 model function to derive its wind.

TOPEX altimeter data comes the TOPEX/Poseidon Merged Geophysical Data Records, generation B ("MGDRB", Benada, 1997 ) for the period of the NSCAT mission, September 1996 to June 1997. Data come directly from the MGDRB CD-ROMs with one exception being that the C-band backscatter data is corrected to remove the Ku-band atmospheric correction and replace this with the proper C-band estimate.

A given colocation point within our data set can be characterized as follows. A valid crossover occurs for time differences of less than +/- 60 minutes and wind cell spatial intersection within +/- 12 km of their respective centers. Data flags for both sensors at that point must indicate deep ocean, no sea ice free and valid data collection conditions. Our resulting data set consists of over 245,000 points.

Next, only those crossover points where the NSCAT midbeam antenna has an incidence angle greater than 40 degrees are kept. This eliminates more than half of the possible ocean crossover points but there is evidence to suggest that near-incidence scatterometer winds are also impacted by the sea state (e.g. Queffelec et al., 1999 ) and so we remove this data. To bring the TOPEX spatial resolution as near to NSCAT as possible we include an average over those TOPEX data points (one point every 6 km along track) that fall within the given NSCAT wind cell. Thus the TOPEX 'wind cell' characteristics become variable from 2 x 6 km to 2 x 25 km. An additional minimal filtering of outliers includes the removal of those points where the TOPEX estimate of backscatter is below 5.0 or above 30.0 dB and those cases where the TOPEX liquid water estimate exceeds 500 microns. The composite data set has a population of 96,500 samples. At each wind vector cell within our data set we have compiled the relevant data collection times, location and relevant supporting data and flagging information to insure data quality. Of course the main parameters at each point are the NSCAT 10 m wind estimate, TOPEX normalized radar cross section ( $\sigma^0$ ) at C- and Ku-band, and TOPEX significant wave height. TOPEX in this case denotes the NASA altimeter aboard the

satellite, we do not use data from the Poseidon altimeter for this study.

### 2.1.2 TOPEX and the ERS C-band scatterometers

The ERS Active Microwave Instrument included a C-band scatterometer that provided another opportunity for TOPEX colocation. TOPEX/ERS crossovers used here were compiled from CERSAT (Centre ERS d'Archivage et de Traitement) products (Cersat, 1996 ). This C-band scatterometer operated with lower incidence angles than NSCAT, and had three antenna but only on one side of the satellite. To encompass the 1996-1997 NSCAT period, and have a statistically representative dataset, we needed to include data using both ERS-1 and 2 satellite instruments over the 2 year period extending from November 1995 to November 1997. The period November 1995 to May 1996 corresponds to ERS-1, with ERS-2 data after this. The scatterometers are identical and their cross-calibration was accounted for within the CERSAT data base.

Processing of the different ERS backscatter measurements results in a wind inversion with surface resolution of 50 km x 50 km. Version 3.2 of the CMOD wind inversion algorithm was used. Only data flagged as free of ice and having valid sensor measurements were kept. No or very low wind (<1 m/s) cases were also removed from the set.

TOPEX altimeter data come from the AVISO CD-ROM, version C. As for NSCAT/TOPEX dataset, C-band backscatter data were corrected to remove the Ku-band atmospheric correction and replace this with the proper C-band estimate. The same additional filtering as for TOPEX/NSCAT was applied.

Colocation was first done for a +/- 60 minute time lag and a +/- 50 km spatial separation. This resulted in more than 300,000 data points. A subset was extracted from this one to keep only those crossovers with 30 min./15 km time and space separations. For a 0 km spatial difference TOPEX ground track size is then about 2 x 100 km. For a 15 km distance it is reduced to 80 km. For a given ERS-2 scatterometer measurement, we then provide two different types of TOPEX measurements: one is for a single point (CD-ROM data), and corresponds to a 2 x 6 km resolution. The other corresponds to a 2 x 80-100 km resolution.

For retrieval of wind speed from ERS-2 scatterometer, all  $\sigma^o$  estimates having their center inside the 50 x 50 km cell are used. This results in a maximum 70 x 70 km ground resolution associated with such a wind speed estimate.

The final data set contains only those cases where all ERS data are for an incidence angle higher than 40 degrees. This leads to a total of 70,500 samples with global coverage. The spatial distribution and density of these crossovers is represented in figure 2b.

### 2.1.3 TOPEX and QuikSCAT

Global Ku-band scatterometer-derived winds from the SeaWinds sensor aboard the QuikSCAT satellite have been available since July of 1999. SeaWinds has two rotating antennas operating at fixed incidence angles (46 and 52 degrees). Colocations of TOPEX and QSCAT data were recently achieved by CERSAT over the three month period from 19 July to 15 October 1999. We note that there had been a substantial change in TOPEX between the NSCAT and QuikSCAT periods in that the original NASA altimeter (side A) aboard TOPEX was switched off and replaced with a redundant system (side B) in Feb. of 1999.

For this data set we selected crossovers with time and space separations of less than 30 min. and 15 km. As with NSCAT, a high resolution processing was applied, resulting in 25 x 25 km wind cells. Taking into account the size of an individual  $\sigma^o$  pattern, the maximum ground resolution associated with the wind estimate should be expected to be significantly higher, close to 50 x 50 km. This product provides two different TOPEX measurement resolutions to remain consistent with the colocated datasets detailed above. The first is the single point MGDR-B data with 2 x 6 km resolution. The second is a 13-second average over the various TOPEX measurements, corresponding to a 2 x 70 km ground cell. Filtering of the two data sources was performed as described for TOPEX/NSCAT with the exception being that all SeaWinds wind vector estimates are for incidence angles above 40 degrees. This data set contains more than 88,000 data points.

### 2.1.4 TOPEX and ECMWF winds

Global model estimates of surface wind vector from the European Center for Medium-range Weather Forecasting (ECMWF) surface analysis are provided for each point in the colocation data sets described above. These model-derived winds will be used for altimeter algorithm validation purposes. We note that the model winds do not come from the ECMWF reanalysis. The ECMWF analysis provides near-surface wind vector estimates for an altitude of 10 m above the ocean and for neutral stability. Their output is on a 1.125 x 1.125 degree grid every 6 hours. For our purpose we interpolate in the model output in space and time to derive a wind estimate colocated with our sensor observations. This results in a maximum time lag of +/- 3 hours. Ground resolution for ECMWF is then 125 x 60-125 km, depending on latitude.

This type of wind product has proven to be quite useful and valid for global development of the average wind characteristics of a sensor such as the satellite scatterometer or altimeter. However the inherent smoothness associated with the relatively larger spatial and temporal scales of such a model does introduce variance into any intercomparison with a finer resolution observation. For example, Freilich and Dunbar(1993) were able to identify a model-related noise factor of 30 % in comparing altimeter and model winds.



### 2.1.5 ERS-2 altimeter and NSCAT

Observations from Ku-band altimeter aboard the ERS-2 satellite can be used for a sort of independent assessment of the work derived using the TOPEX/scatterometer crossover data sets. To this end we obtained the crossovers between the ERS-2 altimeter and NSCAT as produced by CERSAT within its collaboration with NASA and NASDA ADEOS project teams. This compilation covers the whole NSCAT period (CERSAT, 1997; Queffelecoulou, 1999b ). Our data set for validations here was assembled and filtered as for the cases above. A difference here is that NSCAT wind estimates provided are for 50 x 50 km (not 25 km) wind cells. Again, taking into account the size of an individual  $\sigma^\circ$  estimate footprints, the ground resolution associated with the wind estimate may be significantly higher, close to 70 x 70 km. The ERS-2 altimeter measurements are averaged over 11 seconds, representing an along track distance of about 70 km. One-second averaged altimeter measurements are also provided. The total data population contains 129,000 crossovers.

### 2.1.6 GEOSAT altimeter and NDBC buoys

Numerous altimeter wind studies have been conducted using data from the Geosat altimeter. To assess that data and to provide some continuity between studies we obtained the dataset used by Glazman and Greysukh (1993). This compilation matches buoy (of the National Data Buoy Center) and Geosat altimeter measurements for the period November 1986 to July 1989. Data and documentation come from the JPL (Jet Propulsion Laboratory) PO.DAAC web site. The collocation procedure and characteristics are described by Glazman and Pilorz, 1990 . We used data filtering as described by Glazman and Greysukh (1993). Spatial separation is smaller than  $0.5^\circ$  and the time lag is lower than 45 minutes. Geosat  $\sigma^\circ$  and SWH measurements were averaged over three seconds. This data set is much different from the others assembled here in that it is small (less than 5000 points total) and for a very non-global sampling.

## 2.2 Overview of the training data set - NSCAT/TOPEX

Figure 1 presents the TOPEX data versus NSCAT-derived wind speed for the overall data set. Only one tenth of the total colocated samples are represented in the scatter data for panels a,b,c in the figure. As discussed earlier, these complete data represent crossovers for the nine month period from Sept. 1996 to June 1997.

Figure 1a shows Topex  $\sigma_{Ku}^\circ$  measurements in decibels against NSCAT wind speed. Their relation appears to be close to linear above 5-6 m/s, while, with decreasing wind speeds,  $\sigma^\circ$  increases rapidly. One can note that  $\sigma^\circ$  scatter is on the order of 1 dB for a given wind speed. This scatter also increases with decreasing wind speed. An obvious feature of the large data set is measurement across the full range of ocean wind speeds. The overall character of these TOPEX data appear to be entirely consistent with such global TOPEX results as those shown by Callahan et al. (1994) .

TOPEX measurements of significant wave height, SWH, are represented in figure 1b. These data

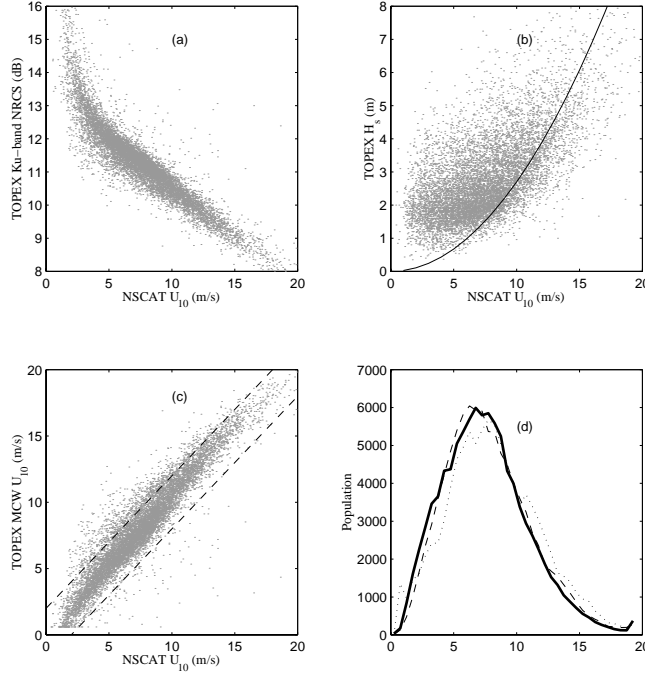


Figure 1: (a) TOPEX Ku-band  $\sigma^0$ , (b) TOPEX Ku-band SWH and (c) TOPEX MCW wind speed - all versus the reference NSCAT 10 m wind speed. Panel (d) provides histograms for  $U_{NSCAT}$  (dashed),  $U_{ECMWF}$  (solid) and  $U_{MCW}$  (dotted)

indicate a broad range of sea state conditions. The model curve on the figure represents fully-developed seas for a given NSCAT wind speed using the Sverdup-Munk model. The wind dependence of these wave height data is also consistent with past global TOPEX observations (e.g. Callahan et al., 1994) where the prevailing interpretation is that the sea state is mostly associated with swell under low wind speed conditions. A broader range of possible wave development states is present at moderate wind speeds. Wave heights below the fully-developed curve likely indicate cases where seas are less than fully developed. However, these occurrences appear much less often in our global data set than do those situations where the sea state indicates presence of both sea and swell. Such mixed swell/sea cases prevail within all of our assembled global altimeter/wind product data sets. The fact that, for light to moderate winds, the background swell is almost always present suggests that ideal fetch-limited wind wave growth situations are a rarity on the open ocean. This appears to be true apart from cases of high wind speeds where the swell energy is a much smaller contribution to the total wave height. For winds above about 11 m/s one can see that the measured wave heights tend nearer to the fully-developed sea prediction. One conclusion we draw here is that a globally-relevant altimeter wind model need not be weighted too strongly toward attempts to correct for fetch-limited situations.

Figure 1c, provides a scatter plot of altimeter wind speed estimated from the operational TOPEX algorithm (Witter and Chelton, 1991), MCW, showing a non-negligible amount of data with wind differences in excess of  $\pm 2$  m/s. We find that for the complete TOPEX/NSCAT data set 15 % of the TOPEX-derived winds exceed these bounds. Furthermore, a systematic overestimation of wind speed by about 0.5 m/s is observed over the whole wind speed range. This bias is confirmed

by the wind speed histograms presented in figure 1d. It has also been pointed out in past studies (e.g. Freilich and Challenor, 1994 ). On panel (d) we also show the wind speed histogram from the collocated ECMWF wind model data. There is excellent agreement between the NSCAT and ECMWF estimation. One obvious but important observation here is that the global wind distributions indicate that the prevailing ocean wind speeds fall between 3 and 12 m/s. This strong weighting of the sampled population towards a mean value of about 7 m/s needs to be considered in wind model developments and validations.

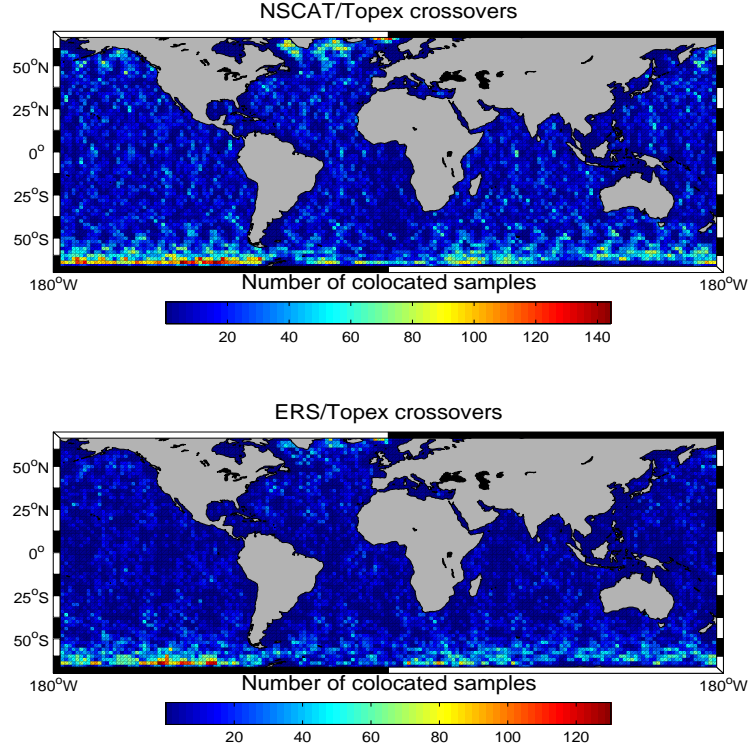


Figure 2: Spatial density of satellite crossover points used in this study. The upper plot is for NSCAT/TOPEX and the lower depicts ERS/TOPEX.

To provide a sense of the global distribution of our compilation we present in figure 2a the spatial density of TOPEX/NSCAT satellite crossover samples for the nine month period. It is apparent that the data set does contain global ocean observations out to the 66 deg. latitude limit of TOPEX. We note that the data of both satellites were conservatively filtered for sea ice occurrence and so this should not be a noise factor in our wind speed studies. A salient characteristic of the crossings for these polar-orbiting platforms was the increased likelihood of high latitude intersections. As one can see in figure 2b this was also the case for the TOPEX and ERS scatterometer intersections. One can note that though the combination was done for two years in the case of ERS vs. nine months for NSCAT the data quantities are similar.

Next we examine the chosen reference wind product for this study - NSCAT's 10 m wind derived from a 25 km wind vector cell. As noted earlier, we restrict our data set to winds derived using scatterometer incidence angles above 40 degrees to ameliorate possible wind speed errors associated with long waves or sea state. For overall validation of the NSCAT winds and the NSCAT-1

geophysical model function see Freilich and Dunbar (1999) , and Wentz and Smith (1999) .

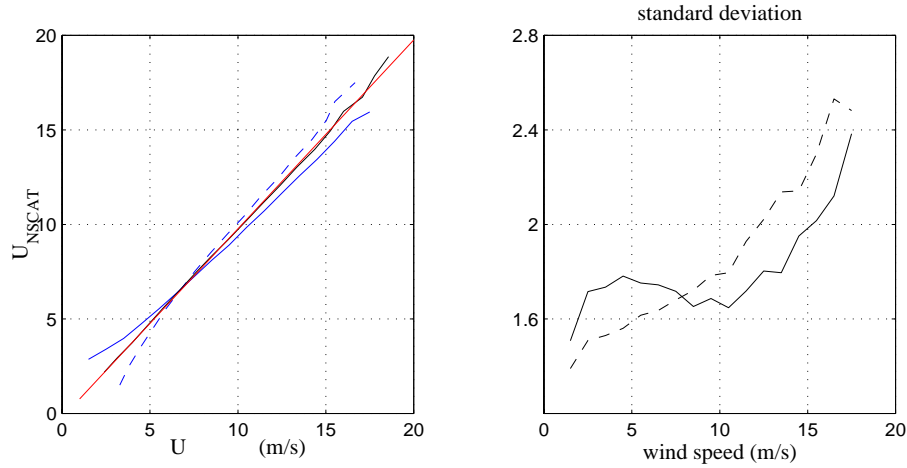


Figure 3: NSCAT and ECMWF wind speed comparisons. (a) upper plot : bin-averaged relations (blue), symmetrical linear regression (red) and identity line (black). (b) lower plot : standard deviation of the  $U_{ns\ cat} - U_{ecmw\ f}$  wind difference, as a function of NSCAT wind (red) and ECMWF wind (black).

Figure 3a presents averaged data and a symmetric linear regression fit between the ECMWF model wind and the NSCAT product. As mentioned earlier the model winds have been interpolated and are a smoother product to begin with. Both products will have substantial rms about a 'true' wind measurement as well as possible biases. A symmetrical linear regression is performed to obtain a result invariant with choice of the regressor. The comparison between the two parameters shows excellent agreement with a slight bias that never exceeds 0.3 m/s in the average of one estimate when averaged over binned subsets of the other. These visible departures of the averaged data from the linear regression reflect a relatively high noise level (see figure 3b) and positive/negative skewness of the distribution at low/high wind. Nevertheless, such bin averaged results appear to be consistent with the symmetrical linear regression as shown in figure 3a.

Referencing figure 3b one sees that standard deviation of the  $U_{NSCAT} - U_{ECMWF}$  wind difference as a function of ECMWF or NSCAT wind speed is about constant at 1.7 m/s for winds less than 10 m/s. For higher wind speeds the rms increases strongly - up to 2.4 m/s at 16 m/s. This increase may be related with: (1) the difference of resolution cells for NSCAT (25 km) and ECMWF (120 km). This becomes more important for stronger winds because they are likely to be associated with smaller scale meteorological structures. (2) the fact that high winds are more likely to be associated with high latitude areas where both NSCAT and ECMWF are not validated. The overall standard deviation between products is 1.8 m/s.

Following sections should make it apparent that intercomparison rms does substantially lower when using colocated satellite measurements as suggested by Freilich and Dunbar (1993) . Data affirm that about 30 % of this 1.8 m/s rms can be readily attributed to the large differences in both space and time resolution between the atmospheric model and the scatterometer.

### 2.2.1 Average SWH impact on altimeter backscatter

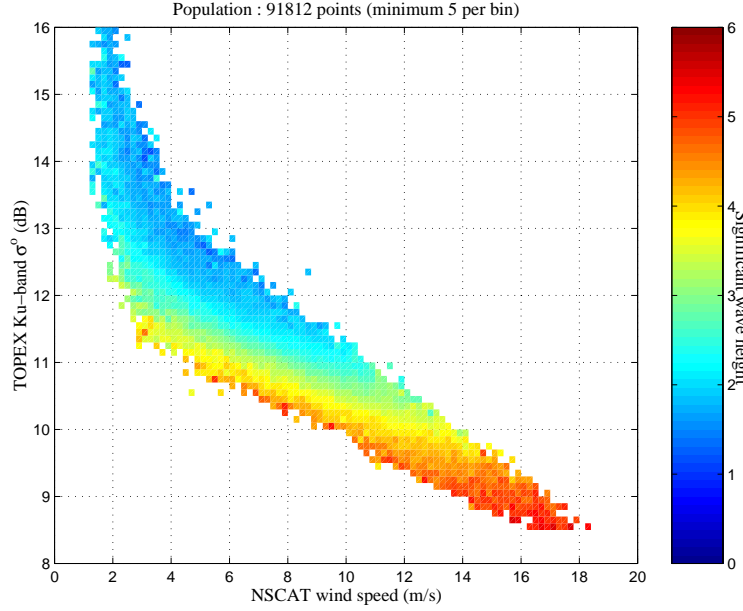


Figure 4: Gridding of the TOPEX  $\sigma_{Ku}^o$  and NSCAT wind speed; color represents corresponding SWH value.

Figure 4 displays a gridding of  $\sigma_{Ku}^o$  versus  $U_{NSCAT}$  with color representing the average value for altimeter-derived SWH for a given wind speed and  $\sigma_{Ku}^o$ . One can observe a clear dependence of altimeter  $\sigma^o$  at constant wind upon SWH variation. The relative magnitude of the change decreases with increasing wind speed. However, the variance is quite strong for common ocean wind speeds, such as the 2 dB range at 6 m/s. Such a 2 dB range translates to large wind error for the TOPEX  $\sigma_{Ku}^o$  wind speed algorithm where wind sensitivity is about 3 m/s/dB at 6 m/s.

It is important to recognize that the pattern that emerges in figure 4 is due to the very large amount and global nature of the assembled data set. Much of the space mapped here represents infrequent events and high latitude observations that would not be seen in smaller and more localized composite data sets (e.g. altimeter collocations with the NDBC buoy network observations). On the other hand, one can expect such a mapping to gain even better definition with a long-term multi-year data collocation where the sampling of sparse regions increases (e.g. TOPEX/JASON-1 and the SeaWinds platforms).

These global observations of an average sea state correlation with altimeter cross section variation for any fixed wind speed confirm, at least in some respects, numerous past studies of sea state impacts on altimeter wind estimations as discussed in our introduction and first suggested by Monaldo and Dobson (1989). One finding in following sections is that the GEOSAT/NDBC data used for many past sea state impact studies shows little of the variations seen in figure 4 and as such, inconclusive findings (cf. Wu, 1999) are not surprising.

Another means of viewing this sea state effect is in terms of the operational altimeter wind product. This algorithm is a straightforward mapping of  $\sigma_{Ku}^o$  to wind speed. Figure 5 provides that result

in panel A versus the ECMWF wind speed. Traces for several ranges of wave height are provided. Here the sea state effect is evident by the TOPEX wind bias above or below the reference wind. We also provide the NSCAT wind for the same wave height ranges to show that indeed the scatterometer wind product shows a negligible relation to the variations in SWH. The ECMWF reference is used to insure direct affirmation that the altimeter exhibits this SWH dependence whereas the scatterometer does not. Results of altimeter wind speed for these SWH ranges and versus the NSCAT wind (not shown) shows a slightly more dramatic departure from the reference wind because there is less intercomparison noise to mask the SWH signal.

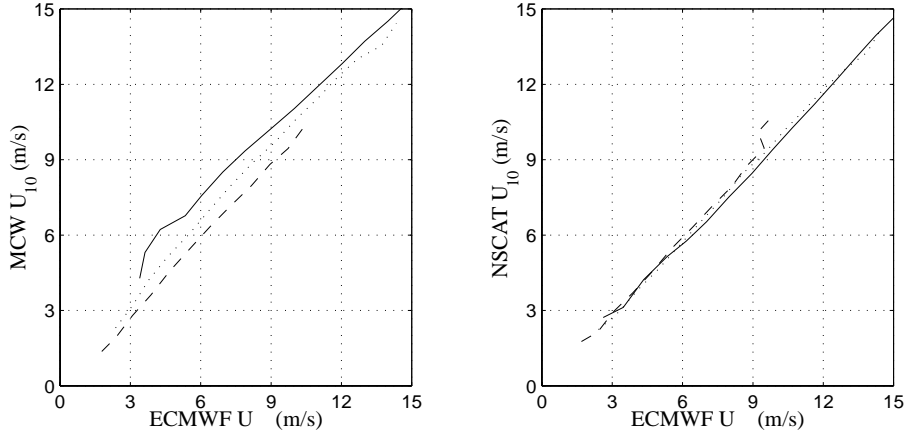


Figure 5: Average relations between  $U_{mcw} - U_{ecmwf}$  (a) and  $U_{nscat} - U_{ecmwf}$  (b) versus ECMWF  $U_{10}$  for different SWH classes : 1m (dashed line), 3m (dotted line), 5m (solid line). SWH range is  $\pm 0.5$  m/s around the indicated value.

Figures 4 and 5 provide motivation for including the altimeter's wave height in attempts to invert accurate wind speed estimates. One could envision a point-to-point altimeter wind speed estimation where both the altimeter backscatter and SWH measurements are used (e.g. Glazman and Greysukh, 1993; Lefevre et al., 1994; Elfouhaily et al., 1997 ). We do caution however that the results shown here depict the average, not the instantaneous, signature. As pointed out in numerous past studies and as expected in our data sets, the wave height parameter will not be a direct indicator of the long wave influences that impact a given  $\sigma_{Ku}^o$  measurement. Just as for the backscatter alone, there is no pairing of  $\sigma_{Ku}^o$  and SWH that uniquely maps to one wind speed. Some ambiguity is likely to remain due to the indeterminate amount of sea versus swell within SWH, the indeterminate direction of the sea versus the swell, unknown fetch etc... This notion that SWH is a limited surrogate for the actual wave conditions should be kept in mind when developing a 2-parameter ( $\sigma^o$  and SWH) wind speed algorithm for the altimeter. A dramatic accuracy improvement with such a model is unlikely, nevertheless, within global considerations the SWH signature of  $\sigma^o$  variations cannot be considered negligible as it is often thought (see Freilich and Challenor, 1994).

Another point to note is that the observation of figure 4 represents a mapping between three variables that is not completely reciprocal. In that figure the average backscatter and wave height are computed for a fixed reference wind speed of NSCAT. Such a result indicates that backscatter can vary substantially for a given wind speed. It is perhaps interesting to notice that when one assesses the inverse case of wind speed variation for a fixed reference  $\sigma^o$  (average the data along y-axis) that the variation's dependence on SWH is much weaker. An initial illustration of this lack of reciprocity

is shown in figure 6 where it is found that the estimated wind speed error is much more correlated when looking at  $\sigma^o$  variation for a constant wind speed (0.53) than the inverted wind speed variation at a constant  $\sigma^o$  value (0.1-0.4). This aspect of the data will be explored further in the following section.

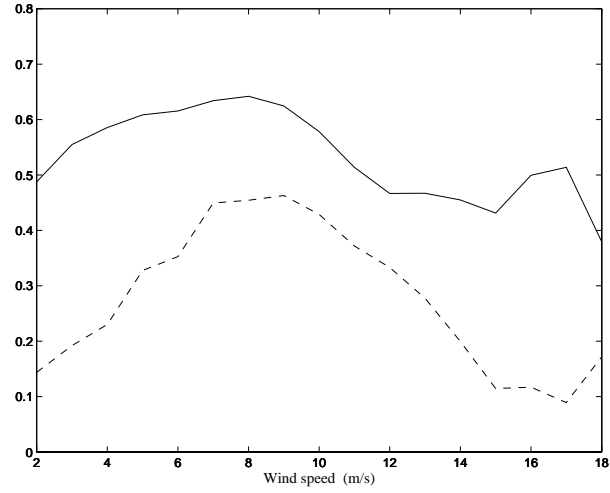


Figure 6: Correlation of the wind speed error  $U_{mcw} - U_{nscat}$  distribution with SWH at a given reference wind speed. The solid trace represents error for case of a constant  $U_{nscat}$  reference while the dashed line is for constant  $\sigma^o$  (or equivalently, constant  $U_{mcw}$ ).

### 3 Ku-band wind speed model functions via neural network methods

Section 2 presented global collocation of the scatterometer and altimeter data depicting that, on average, the altimeter backscatter can be seen as depending on both the near-surface wind speed and significant wave height. As already discussed, this concept is not a new one but the prevailing wind speed retrieval algorithm for the TOPEX and future JASON-1 altimeter mission relies on the standard single parameter Modified Chelton-Wentz mapping (Witter and Chelton, 1991)

$$\sigma_{Ku}^o = f_{MCW}(U_{10}) \quad (1)$$

The MCW routine is still in use because previous two parameter attempts have failed to substantiate the need to include a wave height adjustment (cf. Wu, 1999). Our NSCAT/TOPEX data presents a new opportunity to develop a globally-based altimeter wind speed solution relevant for operational usage. That is, derive the wind speed using solely those two products measured by TOPEX:

$$U_{10} = F_1(\sigma_{Ku}^o, SWH) \quad (2)$$

Referring back to figure 4 one can see that the three dimensional space is somewhat nonlinear, particularly when considering both high and low wind speed regimes. For this reason we chose artificial neural networks to model the relationship between the  $\sigma^o$ -SWH combination and near surface wind speed. This choice assures a robust non-parametric mapping, with one ramification being that a derivative sea state parameter such as pseudo wave age (e.g. Glazman and Greysukh, 1993) that combines wind speed (or backscatter) with SWH should be encompassed by our solution. In the following sections we describe application of two differing neural techniques to the 97,000 realizations of these three parameters in our TOPEX/NSCAT data. The first is a general regression neural network (GRNN) and the second uses the multilayer perceptron (MLP) approach.

The objective in these non-parametric regressions is to generate a globally faithful and continuous representation of the observed relation between our known wind speed and the TOPEX measurements. A most direct means to predict wind speed from the TOPEX observations would be to develop a neural network that provides the forward function  $F_1$  (equation 2). In that case wave height and radar backscatter observation pairs are mapped to a corresponding wind speed. However, from a physical perspective the expectation is that Ku-band  $\sigma^o$  observations are correlated with both the long waves (SWH) and the local wind waves ( $U_{10}$ ). As such, a more physically-relevant development should treat those latter variables as network inputs and  $\sigma^o$  as the output:

$$\sigma_{Ku}^o = F_2(U_{10}, SWH) \quad (3)$$

These functions ( 2) and ( 3) will not necessarily provide identical wind speed values for identical input of the TOPEX backscatter and SWH measurements. In fact our results will show that the solutions are not reciprocal with respect to wind speed mapping and indicative of the relatively high correlation between the radar's backscatter and SWH, especially in comparison to the correlation between NSCAT's wind speed and SWH.



## 3.1 GRNN

### 3.1.1 Network design

A neural network is an association of basic elements called artificial neurons. It can have one or several inputs and outputs, and can be seen as a complex transfer function between inputs  $e_i$  and outputs  $s_j$ .

General regression neural networks (GRNN) are often used for function approximation. It has been shown that, given a sufficient number of neurons, GRNNs can approximate a continuous function to an arbitrary accuracy. GRNNs are comprised of two layers of artificial neurons. The first layer consists of radial basis neurons, whose transfer function is a Gaussian with a spreading factor  $h$ . First layer weights are simply the transpose of input vectors from the training set. A Euclidean distance is calculated between an input vector and these weights which are then rescaled by the spreading factor. The radial basis output is then the exponential of the negatively weighted distance having the form:

$$\Phi(e) = \exp(-\text{dist}(e, w)^2/h^2) \quad (4)$$

Therefore, if a neuron weight is equal to the input vector, distance between the two is 0 giving an output of 1. This type of neuron gives an output characterizing the closeness between input vectors and weight vectors. The weight matrix size is defined by the size of the training dataset ( $m$  parameters  $\times$   $n$  data points), while the number of neurons is the number of input vectors ( $n$ ).

The second layer consists of neurons with a linear transfer function. Weights in this layer can be viewed as the slope ( $m$ ) while the bias vector ( $b$ ) is the y-intercept. Each are solved to minimize the sum-squared error (SSE) between the output of the first layer ( $x$ ) and desired output ( $y$ ).

As the spreading factor  $h$  increases, the radial basis function decreases in width. The network will respond with the target vector associated with the nearest design input vector. As the spreading factor  $h$  becomes smaller, the radial basis function increases in width. Several neurons may then respond to an input vector. This is because the network does a weighted average of corresponding target vectors. As radial basis function gets wider and wider, more neurons contribute to the average resulting in a smoother model function. For this study, the spreading factor was held constant for all neurons and is optimized through calibration of the network.

One advantage of the GRNN approach is simplicity. The adjustment of only one parameter  $h$  is sufficient for determining the network. Drawbacks of this technique can be the large network size and computational cost associated with developing this network for a large set of input test vectors such as our NSCAT/TOPEX data set. To adequately characterize the training data it is typical that the number of neurons equals the number of training vectors. As the number of training vectors increases, the network size and computational load increases. Our approach in implementing

a GRNN solution is to reduce the number of training vectors. One notable implicit feature of the GRNN solution is that the solution is not in compact or closed form. The function is essentially a look-up table of the networks coefficients with matrix size equal to the training set.

### 3.1.2 Input dataset

For reasons discussed above we chose reduce the number of input training vectors by developing a grid that presented the average response of the inputs to the output. Two separate training grids were created to solve  $F_1$  and  $F_2$ , ( 2) and ( 3) above.

**( $\sigma^\circ$ ,SWH) training grid -  $F_{1GRNN}$**  At each grid point, an average wind speed was computed based on the peak of the wind distribution. The grid was defined as running from 6.5-25 in  $\sigma^\circ$  and 0.5-6. in SWH with step size of 0.1 dB in  $\sigma^\circ$  (0.2 dB for  $\sigma^\circ$  above 12 dB) and 0.25 m in SWH. The distribution peak was chosen due to the non-normal distribution of wind within grid cells at low and high wind speeds. Since data is near normal in central grids, the peak equals the average and therefore our training input grid is consistent across all elements. Values are only allowed into the training grid if an element (unique pairing of SWH and  $\sigma^\circ$  ) contains at least 7 samples. Thus there will not be a GRNN solution for the sparsest regions of the data set, such as low values for both  $\sigma^\circ$  and very low SWH.

**( $U_{10}$ ,SWH) training grid -  $F_{2GRNN}$**  Data were dispatched on a (wind speed, SWH) grid where for each grid element a characteristic  $\sigma^\circ$  value was calculated. The grid was defined as running from 1-19 in  $U_{10}$  and 0.5-6. in SWH with step size of 0.2 m/s in  $U_{10}$  and 0.25 m in SWH. In this case the distribution of  $\sigma^\circ$  values for a given element is close to normal over the entire grid. Therefore we characterize the distribution of  $\sigma^\circ$  by its mean if a sufficient number of points are found. As above, sparse elements with few or no samples are omitted.

### 3.1.3 Model training and optimization

In the case of the GRNN, the first training step consists in setting weights of both layers of the network respectively to inputs and outputs of the training dataset. The remaining step then is to optimize the spreading factor  $h$  by use of a calibration dataset which is separate from training set. Since an averaged data grid was used for the training vectors, we select different raw subsets from our global dataset for calibration. An optimal value for  $h$  is then determined and used for training. Any use of the network subsequent to training maintains this value of  $h$ .

As mentioned, the Euclidean distance is measured between inputs and weights of the first layer. To give each variable equal weighting in the inversion we normalize all three variables before training.

## 3.2 MLP

### 3.2.1 Network design

A multilayer perceptron (MLP) is a well documented neural architecture that when combined with backpropagation of errors provides a powerful and compact solution to many intractable problems [Hagan et al. 1996] [Sterling and Pollack 1996]. For this study, we find adequate characterization using a three layer MLP consisting of an input layer, a single hidden layer, and an output layer. Two nodes represent the two inputs ( $U_{10}$  and TOPEX SWH for  $F_{1MLP}$  or TOPEX  $\sigma^o$  and SWH for  $F_{2MLP}$ ). The hidden layer has two nodes and the output layer has one ( $U_{10}$  or  $\sigma^o$ ). A log-sigmoid transfer function of the form:

$$f(net) = 1/(1 + \exp(-net)) \quad (5)$$

is used between both the hidden and output layers. The requisite rescaling of all input and output variables is made to normalize the data between .1 and .9 due to the asymptotic limits of this function.

Advantages of the backpropagation MLP include a small solution network and quick (forward) computational speed that permits training over a large input vector set. The main disadvantage of the backpropagated MLP is the many variables which must be considered when constructing a MLP. This includes the number of hidden layers, the type of transfer function(s), the initial conditions, and the types of backpropagation MLPs available. One must also consider the training time which is a direct function of training set size and MLP chosen for the task.

### 3.2.2 MLP training and optimization

The MLP network developed here is not trained in the traditional manner of dividing the set in two and using one set for training and the other set for independent testing. This is due to the sparse distribution of data at the extremes in the grid and how these points are under-represented during neural training. Since a function's sensitivities (partial derivatives with respect to all network weights and biases) are added during training (Hagen et al.), large differences in data distribution across the training domain can potentially lead to solutions that are biased towards higher density regions. For the TOPEX/NSCAT data set it is clear from the wind speed distributions shown in section two that there are many more training samples near 7 m/s than, for example, near 2 or 18 m/s. In turn, it was empirically determined that the non unique nature of the proposed mapping between these three chosen parameters leads to a solution that favors minimization near the densest data population at the expense of low and high wind regimes. To help alleviate this feature, we equalize the distribution of points placed into the training set. This involves 'binning' the data into 41 equally spaced wind speed bins of spanning from 0-20 m/s. Only 200 randomly-selected sample data pairs from each bin are allowed into any given training vector set. Any bin with fewer than 200 samples has all its points included. Therefore, all data at the extremes are included in any given training set

and the MLP solution weighting towards  $U_{10}=7$  m/s is lessened. An added benefit of this training set conditioning is a reduction in the training set size from the initial 97000 sample pairs. This size reduction enables holding aside a large portion of the data set for validation and permits use of the following backpropagation technique.

An enhanced error backpropagation technique called the Levenberg-Marquardt algorithm is used to increase training speed. Our method of training is to search for an optimized solution by creating a network for random draws of our equalized training subset (5% of the total set), each subset chosen as described above. For each training set the Levenberg-Marquardt algorithm is run for 50 epochs. At this point, training is halted and a 'goodness-of-fit' ([Kohler 1988]) test is made to check for solution improvement using a Chi-Square test statistic of the form:

$$K = \sum ((fo - fe)^2) / fe \quad (6)$$

where -

$fo$  = observed or neural calculated wind distribution  $fe$  = expected or known wind distribution

The Levenberg-Marquardt algorithm itself does a good job of reducing the MSSE (mean sum squared error). For almost any randomly drawn data set the MSSE will converge to nearly the same minimum value. However, what we desire in this case is both this minimization of the global error variance as well as minimization of the error bias and skewness across the whole range of wind speeds (or  $\sigma^\circ$  for  $F_2$ ). This additional step of computing a Chi-Square test statistic between the known and neural-calculated distributions serves as an additional optimization criterion to the Levenberg-Marquardt training. The combined Chi-Square 'goodness-of-fit' and MSSE optimizations lead to computed and known data distributions that are equalized and a solution where bias and variance variation are minimized.

Resulting solutions for  $F_1$  and  $F_2$  consist of nine coefficients. Their values and the details on algorithm implementation are given in a later section.

### 3.3 Results

We arrive at four separate neural network solutions after training to solve  $F_1$  and  $F_2$  using both the GRNN and MLP approaches. In the following, we will denote the type of neural method used with low indices ( $F_{1MLP}, F_{1GRNN}, F_{2MLP}, F_{2GRNN}$ ). Brief comparison between these models will primarily be made here via reference to altimeter-estimated wind speed using the TOPEX measurements as input ( $\sigma_o, SWH$ ). The 10 m wind speed is directly obtained from  $F_1$  but must be inverted when using  $F_2$  (i.e. an interpolated look-up table was used in this case). A more thorough evaluation of our two parameter approaches will be provided in a validation section to follow.

As a first illustration of the models we present their response versus altimeter backscatter and versus wind speed for three separate values of significant wave height. Each model panel in Figure 7

also shows the standard TOPEX wind speed routine, MCW. The upper panels in the figure show the respective TOPEX/NSCAT observations as extracted from the averaged, binned data grids that are used to train the GRNN solutions. These averaged values depict the desired goal for our solutions and it is apparent that all four approximations do carry information on the SWH parameter consistent with those observations. The observations and models make it quite clear that  $F_1$  and  $F_2$  present substantial differences with respect to wave height impacts in wind inversion. This is consistent with our physical expectations (see figure 6 and related text regarding SWH correlations) that  $F_1$  model functions will result in lower SWH dependency of altimeter  $\sigma^o$  than  $F_2$  for a given wind speed. This is particularly evident at the low and high wind speeds.

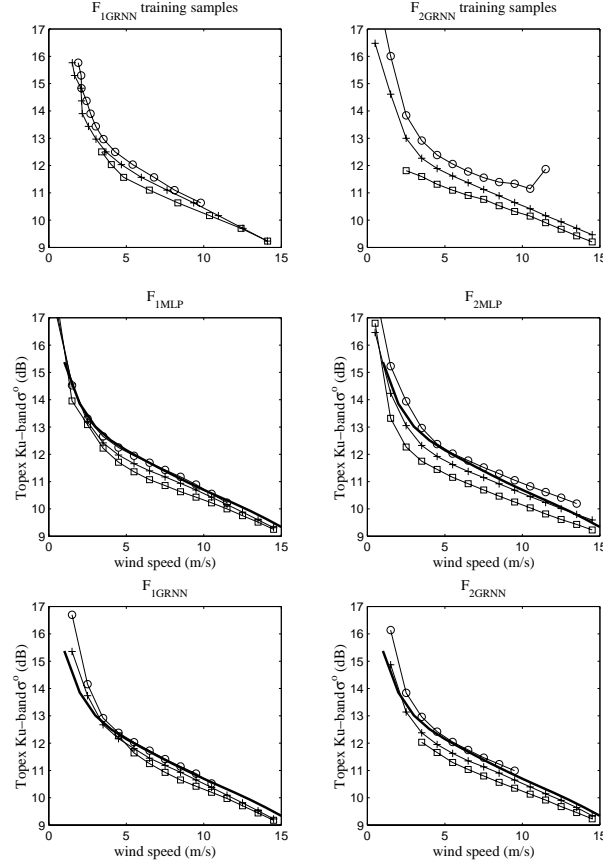


Figure 7: Top left (right) panel represents the averaged data used for  $F_{1GRNN}$  ( $F_{2GRNN}$ ) training. Average behavior of the 4 neural models are also presented, middle panels for MLP, bottom panels for GRNN. Three different SWH classes were selected : 1m (circles), 3m (pluses) and 5m (squares). MCW model is represented for comparison (thick line).

Wind speed histograms of wind speed from the four neural models are presented figure 8. In each case, NSCAT wind speed histograms are overplotted for comparison. MLP models produce smoothly varying histograms that closely resemble the NSCAT observations. This is not surprising as MLP solutions were optimized in part to minimize histogram differences. GRNN histograms do differ from NSCAT, and, as claimed by Freilich and Challenor (1994), this is a potential weak point of GRNN techniques. However, the  $F_{2GRNN}$  histogram does not present large distortions.

As a further illustration of the present solutions figure 9 presents a scatter plot comparing neural-

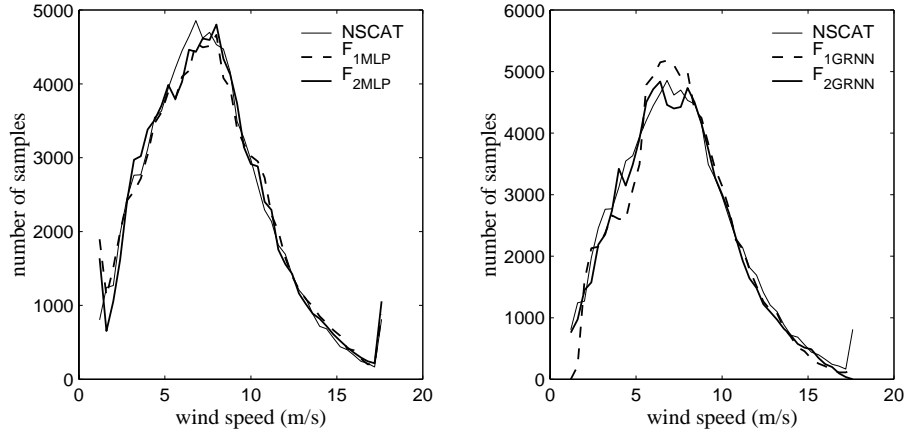


Figure 8: Histograms of neural wind speeds in the NSCAT/Topex dataset. Left plot concerns MLP, right plot concerns GRNN. On each plot are represented :  $F_1$  (thick dashed),  $F_2$  (thick full line), NSCAT (thin full line).

derived altimeter wind speed(using  $F_{2GRNN}$  as an example) to the reference NSCAT wind speed in the  $(\sigma^\circ, U_{10})$  space and for a random subset of the 97000 data samples. One can see that our computation provides a range of  $U_{10}$  estimates for a given  $(\sigma^\circ)$  that accords well with the NSCAT estimates. We can also point out figure 9 that the standard deviation of wind error is visibly improved. Note that both the GRNN and MLP solutions can be justifiably validated using the overall TOPEX/NSCAT data set because their respective training did not depend on the entire data set.

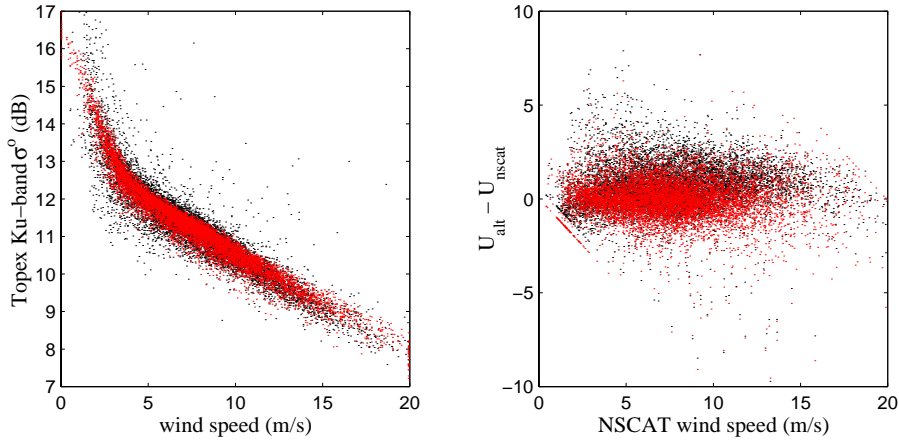


Figure 9: Left : scatter plot of altimeter Ku-band  $\sigma^\circ$  and as function of wind speed. Black dots correspond to NSCAT wind speed, red dots to  $F_{2GRNN}$ . Right : scatter plot of altimeter error wind speed (relatively to NSCAT estimate) as function of NSCAT wind speed. Black dots correspond to MCW, red dots to  $F_{2GRNN}$ .

Referring back to Figure 7 the two selected neural techniques provide solutions that are quite similar for the case of both  $F_1$  and  $F_2$ . Both MLP and GRNN models smoothly cover the space. One can note those regions where there is no GRNN solution due to the lack of data points. For the case of  $F_1$  the two techniques appear to yield very similar results with respect to SWH dependence with the exception of some slight difference for wind speeds below 5 m/s.

Light wind is in some sense a special case for both the  $F_1$  and  $F_2$  spaces and both network tech-

niques. This is partly because the altimeter backscatter and scatterometer winds become highly variable at light winds and partly because there is a limited amount of data on which to train for those rare events such as low wind and high wave height (e.g.  $U_{10} = 1$  m/s and SWH=5 m). The altimeter backscatter can span an uncharacteristically large range (from 13 to 28 dB) for the case of no to light wind with no clear dependence on wave height. The GRNN will differ from the MLP for light winds because the GRNN optimizes only about a proximity to the respective solution grid point while the MLP attempts to perform a least square solution over all the presented training vectors. In any case, one can see that the  $F_1$  solutions do accord well with the single parameter MCW near light winds.

The global nature of the spreading factor  $h$  in the GRNN solution for  $F_2$  is the likely determinant for most of the difference between MLP and GRNN solutions for this mapping as seen in Figure 7. Comparison to the upper panel observations in that figure suggest that the MLP model provides a closer reproduction of the average impact of SWH on the altimeter. At almost all wind speeds it appears that the SWH signal is more dynamic. In particular at high winds, where the sensitivity of backscatter to wind speed becomes shallowest, it is likely that the globally-defined spreading factor in the GRNN training was large enough that the dynamics of the SWH signature were somewhat smoothed out resulting in a lower weighting for the sea state impacts.

Further evidence of similarities and differences is given in figure 10 showing the 2D probability density function of  $\sigma^\circ$  and SWH at a two fixed wind speeds (5 and 10 m/s). Each plot shows the behavior of the four neural models versus wave height. Of course, the MCW altimeter model represented on this plot would give a vertical straight line. It is apparent that  $F_2$  models are more efficient than  $F_1$  ones in reproducing the SWH dependence of  $\sigma^\circ$  at constant wind speed, both at  $U_{10} = 5$  and at 10 m/s.

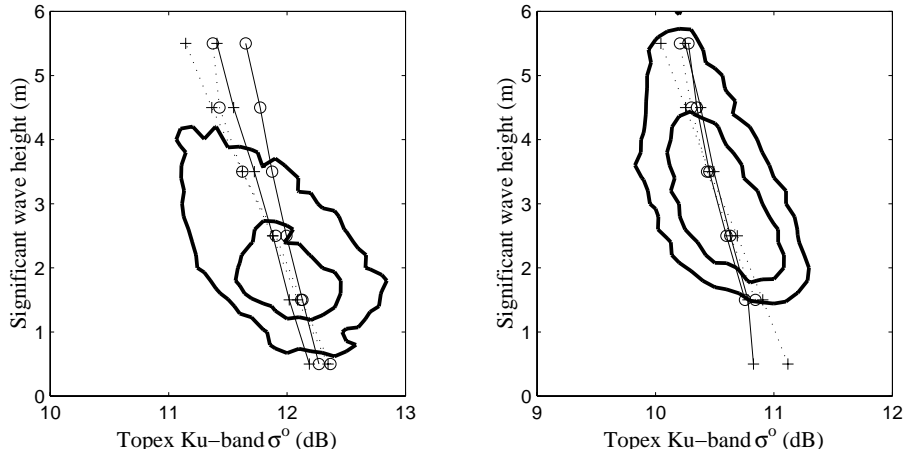


Figure 10: Bidimensional probability density function of  $\sigma^\circ$  and SWH at a constant NSCAT wind speed. Left plot is 5 m/s, right plot is 10 m/s (+/- 1 m/s). Contour plots are given for two values, one twentieth and one fourth of the maximum of the probability density. Traces show the behavior of the four neural models. See the following figure for legend.

A final illustration provides each model's dynamic range for Ku-band backscatter variation given a corresponding range of wave height (in this case 4.5 m). This is provided versus wind speed as shown in figure 11 where the range of NRCS variation changes as a function of wind speed, as

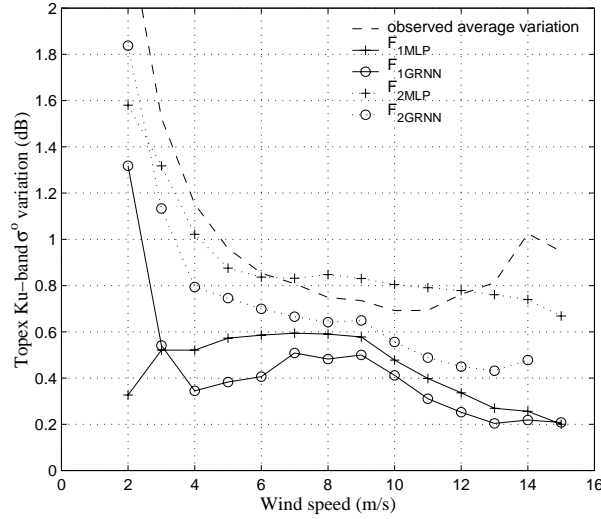


Figure 11: Global TOPEX Ku-band  $\sigma^o$  variation associated with a SWH variation of 3.5 m. The specified range is changing with wind speed. Results are presented for NSCAT wind speed and the 4 neural models.

predicted via the different algorithms, and observed in the bin averaged TOPEX/NSCAT data. As wind speed increases, we shifted the SWH range towards higher values (centered on mean value). One observes that in for case of  $F_1$  models the predicted  $\sigma^o$  variations with SWH are lower (0.4-0.6 dB for a 4.5m SWH variation at 5 or 10 m/s) than with  $F_2$  models (0.9 dB at 5 m/s, 0.6-0.8 dB at 10 m/s). This is especially true for wind speeds lower than 5 m/s or higher than 10 m/s. Referring to figure 6 in section 2 should serve as further clarification. We recall that 0.5 dB variations translate to about a 2 m/s wind speed variation for single parameter algorithms.

Algo	bias	std	rms	% error > 2 m/s	U error trend	Hs error trend
$F_{1MLP}$	0.05	0.98	0.98	4	-0.00	0.23
$F_{1GRNN}$	0.17	0.94	0.95	4	-0.08	0.09
$F_{2MLP}$	0.04	1.01	1.01	5	-0.01	-0.00
$F_{2GRNN}$	0.08	0.95	0.95	4	-0.05	0.02

Table 1: Statistical characteristics of our neural Ku-band altimeter wind speed algorithms, averaged over the whole wind speed range.

One can note that between 6 and 12 m/s,  $F_{2MLP}$  is slightly overestimating the SWH impact on  $\sigma^o$  by less than 0.1 dB but otherwise this model is the closest reproduction of the observations.

Finally, we provide a quantitative comparison between the four solutions in terms of altimeter wind speed error with respect to reference NSCAT values. Tables 1 and 2 some statistical characteristics for these Ku-band algorithms. The U and  $H_s$  error trends are simply the slope of the linear fit between these parameters and the computed wind errors. Two tables are provided to give the statistics computed over the complete wind speed range but also at specific wind speeds to elucidate the wave



<b>Algo</b> <b>3-5 m/s</b>	<b>bias</b>	<b>std</b>	<b>rms</b>	<b>% error</b> <b>&gt; 2 m/s</b>	<b>Hs error</b> <b>trend</b>
$F_{1MLP}$	0.10	1.04	1.05	6	0.52
$F_{1GRNN}$	0.50	0.99	1.11	8	0.51
$F_{2MLP}$	0.16	0.96	0.97	5	0.19
$F_{2GRNN}$	0.32	0.94	0.99	5	0.21
<b>7-9 m/s</b>					
$F_{1MLP}$	0.03	0.95	0.95	4	0.30
$F_{1GRNN}$	0.04	0.85	0.85	2	0.28
$F_{2MLP}$	-0.01	0.95	0.95	4	-0.02
$F_{2GRNN}$	-0.00	0.91	0.91	3	0.07
<b>11-13 m/s</b>					
$F_{1MLP}$	0.09	1.03	1.03	4	0.41
$F_{1GRNN}$	-0.14	0.98	0.99	3	0.43
$F_{2MLP}$	0.01	1.18	1.18	6	-0.12
$F_{2GRNN}$	-0.05	1.05	1.05	4	0.25

Table 2: Statistical characteristics of our neural Ku-band altimeter wind speed algorithms, for 3 wind speed ranges, 3-5, 7-9 and 11-13 m/s.

height dependence. We also note that all data are not included in the calculations. Those input data pairs where the GRNN solutions do not exist were omitted.

One can note that all algorithms provide bias values that are generally well below 0.2 m/s. Wind speed error trends are systematically low, showing that bias is not varying with wind speed. The standard deviation (std) values for the various routines and wind speeds fall within about 5% of one another excepting a departure to higher values by  $F_{2MLP}$  at 11-13 m/s. The  $H_s$  error trends, or lack thereof are best seen in Table 2. Here one observes that  $F_2$  models were able to fully account for the systematic  $\sigma_{Ku}^o$  variations with  $H_s$  especially for moderate wind speed range where most data fall. The  $F_1$  models still exhibit some slope indicating that some error still resides due to that parameter. Overall, it is apparent that the GRNN and MLP approaches are giving similar results, with the GRNNs providing slightly lower rms values.

Succinct summary of the neural network developments finds that the addition of SWH in mapping between ocean wind speed and Ku-band altimeter backscatter will lead to some modification of altimeter wind speeds. Distinct differences arise depending on the choice of mappings - i.e. a decision to resolve the correlation between wind and SWH ( $F_1$ ) or between  $\sigma_o$  and SWH ( $F_2$ ). The two selected neural techniques provide solutions that are quite similar for the case of both  $F_1$  and  $F_2$ .

We recall that use of GRNN requires a two dimensional look-up table, that is a large number of parameters, while the MLP is a globally-applicable closed form solution using 10 parameters (6 scaling constants and 4 computational parameters). In addition, GRNN functions were not trained

on the whole input space and do not provide an answer for some low population density areas of the input dataset. As both neural methods provide similar results, we decide to focus solely on the MLP solutions for operational application and validations. Our MLP solutions  $F_1$  and  $F_2$  are described in annexe A. Evaluation of their effectiveness as altimeter wind speed routines follows.

## 4 Validation and model comparisons

Observations and altimeter model developments of the previous sections suggest that a two parameter algorithm may lead to improved Ku-band altimeter wind speed estimates. Quantitative improvement is assessed here by intercomparison of the proposed non-parametric models of section three (  $F_{1MLP}$ ,  $F_{2MLP}$  ) with previously published altimeter models. Several past studies on altimeter ocean wind speed models have emphasized the point that the sole standard for algorithm comparison should not simply be the global reduction of the root mean square (rms) wind speed error (cf. Glazman and Greysukh, 1993). A key objective in this study is to provide an altimeter wind speed algorithm with the best overall statistical performance when applied to global open-ocean observations. We consider this objective to be in line with the development of an operational algorithm (i.e. geophysical model function, GMF) for use in point-to-point wind speed estimates under all possible combinations of altimeter backscatter and wave height encountered on the open ocean. We note that, for the case of the two parameter altimeter routine, our criterion of global application appears to necessarily limit the utility of such a wind retrieval for 'special cases' such as coastal or fetch-limited studies. Further discussion of this point will be made later on in our summary.

The large amount of data in our training (TOPEX/NSCAT) and numerous validation data sets allows us to estimate wind error measures with very high confidence levels. This includes the ability to assess wind speed errors at light, moderate and high wind speeds as well as the identification of wind speed error trends versus reference wind speed and versus SWH. Evaluation criteria include the minimization of wind speed error bias as well as the rms. Due to operational and climatological study considerations we also desire a continuous function and one that provides a faithful global wind speed histogram.

There are many published models to derive altimeter wind speed using solely the Ku-band radar backscatter. We limit our choice of single-parameter algorithms for intercomparison to the models of Brown et al. (1981), Witter and Chelton (1991) and Freilich and Challenor (1994). We denote these in the following text as B81, MCW, and FC, respectively. Our contention is that these routines encompass most other variations - B81 represents a buoy-tuned three wind regime function that often seems to produce lowest global rms whereas MCW and FC represent smoother, statistically-derived functions that seem very closely related. The MCW routine is used to produce the wind speeds reported by the TOPEX altimeter on an operational and global basis. As a review, we recall that Chelton and Wentz (1986) used Seasat altimeter measurements of radar cross section and 200 km removed Seasat scatterometer (SASS) estimates of wind speed to build an altimeter wind model function. MCW modified this relation for use with Geosat altimeter by comparing Seasat and Geosat globally-derived altimeter  $\sigma^\circ$  histograms. MCW is provided as a look-up table for 10 and 19.5 m height wind speeds.

We also assess two wind speed models that utilize both the Ku-band  $\sigma^\circ$  and SWH. Lefevre et al. (1994) provides a closed-form parametric solution as a function of the two altimeter measurements based on comparison of the TOPEX altimeter data to the ARPEGE (Meteo- FRANCE atmospheric model) wind model data. Glazman and Greysukh (1993) developed a classification approach where wind speed is estimated using one of two distinctly separate single parameter ( $\sigma^\circ \rightarrow U_{10}$ ) mod-

els. This work was based on comparisons between buoy-derived wind and wave data and Geosat altimeter measurements. For operational use (we term this algorithm GG2) this classification calls on use of the individual wave height and  $\sigma^\circ$  estimates. The classification is rooted in the concept of pseudo wave age,  $\zeta$  ( $\zeta = f(SWH/U^2)$ ), where one of their algorithms pertains to 'young' or fetch-limited wind wave conditions and the other to all other cases (i.e. covering fully-developed seas as well as mixed sea and swell). Having only two sea state classes, their algorithm will likely lead to bimodal wind speed distribution for a given  $\sigma^\circ$ . To attenuate this effect they used slightly overlapping pseudo wave age (or SWH) classes.

We now present model comparisons, first utilizing the TOPEX/NSCAT data set. Recall that though these data were used to develop our neural network functions, the MLP training method only required less than 10% of the data. Thus we can still utilize this data for model assessment. Next, to assure independent validation and to provide some sense of factors such as intercomparison noise and sensor calibrations, the algorithms are assessed using the seven additional colocation data sets described in section two. These tests include using the Geosat and ERS-2 altimeters in place of TOPEX, and wind speed surface truth from C and Ku-band scatterometers, ECMWF and the NDBC buoy network.

## 4.1 TOPEX wind speed estimates versus NSCAT

The colocated altimeter and scatterometer data from TOPEX and NSCAT have been discussed in previous sections. We only recall that we expect this is our best available data set for assessing the sea state impact on the altimeter wind speed due to the small scatterometer footprint (25 km cells) and apparent lack of sea state impact on the scatterometer winds for the chosen outside incidence angles greater than 40 degrees (see fig. 5). In the following, we systematically restrict our evaluation of wind speed differences to reference wind speeds falling between 1 and 17 m/s. This range of validity seems to encompass the range of conditions over which most of the models were developed. We also note that, where applicable, TOPEX backscatter values are adjusted down by 0.63 dB for use in Geosat era routines (see Callahan et al., 1994).

We define the wind speed difference,  $U_{err}$ :

$$U_{err} = U_{10altimeter} - U_{10reference} \quad (7)$$

where the reference is NSCAT in this case and winds are in m/s. Wind error standard deviation is simply:

$$std = (\langle u_{err}^2 \rangle - \langle u_{err} \rangle^2)^{\frac{1}{2}} \quad (8)$$

This factor will be of some value in providing a relative algorithm assessments but is obviously equivalent to the rms when the bias nears zero.

Algo	bias	std	rms	% error > 2 m/s	U error trend	Hs error trend
B81	0.36	1.16	1.22	9	-0.22	-0.04
MCW	0.61	1.19	1.34	12	0.03	0.48
FC	0.02	1.22	1.22	7	0.03	0.48
GG2	0.04	1.07	1.07	5	-0.06	0.17
Lefevre	0.28	1.44	1.47	15	-0.28	0.17
$F_{1MLP}$	0.04	1.05	1.05	5	0.00	0.20
$F_{2MLP}$	0.01	1.10	1.10	6	-0.02	-0.06

Table 3: Some characteristics of wind speed error estimate from Ku-band altimeter data using several different algorithms. Data come from the colocated dataset TOPEX-NSCAT, with 96436 samples. Only samples for which all algorithms are defined were used. Altimeter data are from Topex, and reference wind speed is given by NSCAT. The wind speed range is 1 to 17 m/s.

Tables 3 and 4 present the  $U_{err}$  for the various algorithms mentioned above. Table 3 shows some statistics for the commonly-cited case where all wind speed values are included. A first observation is the general level of about 1.0 - 1.4 for the rms error. This is quite low compared to past published values of 1.6 to 2.0 associated with buoy or model wind comparisons. This change in noise level is most likely the strong decrease in spatial collocation distance and spatial sample size. Such numbers are in accord with studies where the spatial separation is limited to 15 or 20 km (e.g. Hwang et al., 1998). Note that the sample population here is more than 96000, thus parameter noise levels are negligible.

Next one can see that the overall bias numbers for all the chosen routines is well below 1 m/s with only the MCW algorithm showing a value above 0.5. We included the trend of the wind speed error versus wind speed to provide some indication of the bias variability with wind speed. As one can see, B81 and Lefevre model bias trends are much higher than for the other routines. The most commonly reported parameter, global rms, shows values spanning from 1.05 to 1.47. It is clear here that the Lefevre algorithm has a substantially elevated error. The single parameter models (B81, MCW and FC) exhibit similar rms and std estimates (1.2) while the three two parameter algorithms (GG2,  $F_{1MLP}$ ,  $F_{2MLP}$ ) are below 1.10.

Table 3 also provides a column representing the wind error versus SWH for consistency with Freilich and Challenor (1994) but we suggest that this parameter is of limited meaning and a much clearer picture emerges when viewing that error trend for specific wind speed ranges as in Table 4. We present estimates at wind speeds of 4, 8 and 12 m/s to provide the sampling near the most populated mid- range wind region and for low and high winds where there are still a substantial data population. In addition, we provide Figure 12 showing wind error bias and standard deviation (std), root mean square wind error (rms) and the linear regression correlation coefficient (R) for the trend of error versus SWH. These parameters are presented for all the forementioned algorithms and for the range of NSCAT reference wind speeds shown.

Algo	bias	std	rms	% error > 2 m/s	Hs error trend
<b>3-5 m/s</b>	15894 samples				
B81	1.20	1.02	1.57	16	0.72
MCW	0.62	1.28	1.43	13	0.91
FC	-0.04	1.24	1.24	9	0.89
GG2	0.43	0.92	1.01	6	0.61
Lefevre	1.52	1.08	1.87	26	1.05
$F_{1MLP}$	0.09	1.07	1.07	7	0.50
$F_{2MLP}$	0.15	0.99	1.00	6	0.17
<b>7-9 m/s</b>	22602 samples				
B81	0.30	0.81	0.86	3	0.50
MCW	0.59	1.14	1.28	12	0.78
FC	-0.03	1.14	1.14	7	0.78
GG2	-0.15	1.14	1.15	7	0.26
Lefevre	-0.12	1.07	1.08	6	0.99
$F_{1MLP}$	0.04	1.00	1.00	5	0.26
$F_{2MLP}$	-0.02	1.01	1.01	5	-0.05
<b>11-13 m/s</b>	8311 samples				
B81	-0.84	0.91	1.24	6	0.38
MCW	0.85	1.19	1.46	14	0.53
FC	0.28	1.23	1.26	7	0.56
GG2	0.01	1.12	1.12	5	0.44
Lefevre	-0.88	1.20	1.49	15	0.93
$F_{1MLP}$	0.06	1.15	1.16	5	0.28
$F_{2MLP}$	-0.07	1.36	1.36	10	-0.26

Table 4: Similar to the preceding table with narrower wind speed range. This range is specified in the table.

We first discuss the single parameter routines. Referring to Table 4 and Figure 12 we see that Brown's algorithm appears to have a relatively low rms behavior in the range of 7-9 m/s, where it produces the lowest wind error rms. But variation comes for other wind ranges, where it presents strong bias, low winds being overestimated and high winds underestimated. The B81 bias variation is responsible for this large increase in wind error rms below 7 m/s and above 11 m/s. Furthermore, we find that B81 presents significantly lower wind error standard deviation than the other single parameter algorithms. This feature is again related to a strong wind speed dependence in the wind error bias within the chosen wind bin, varying 0.5 m/s on a 2 m/s-wide bin. We see that in table 3 we obtain a  $-0.22$  m/s wind speed error trend. As soon as bias increases more slowly with wind speed (at low and high wind),  $U_{alt}$  standard deviation increases towards values obtained from other single parameter algorithms. These observations seem completely consistent with Freilich and Challenor (1994) who noted that the chosen three branch form of the Brown model leads directly to these

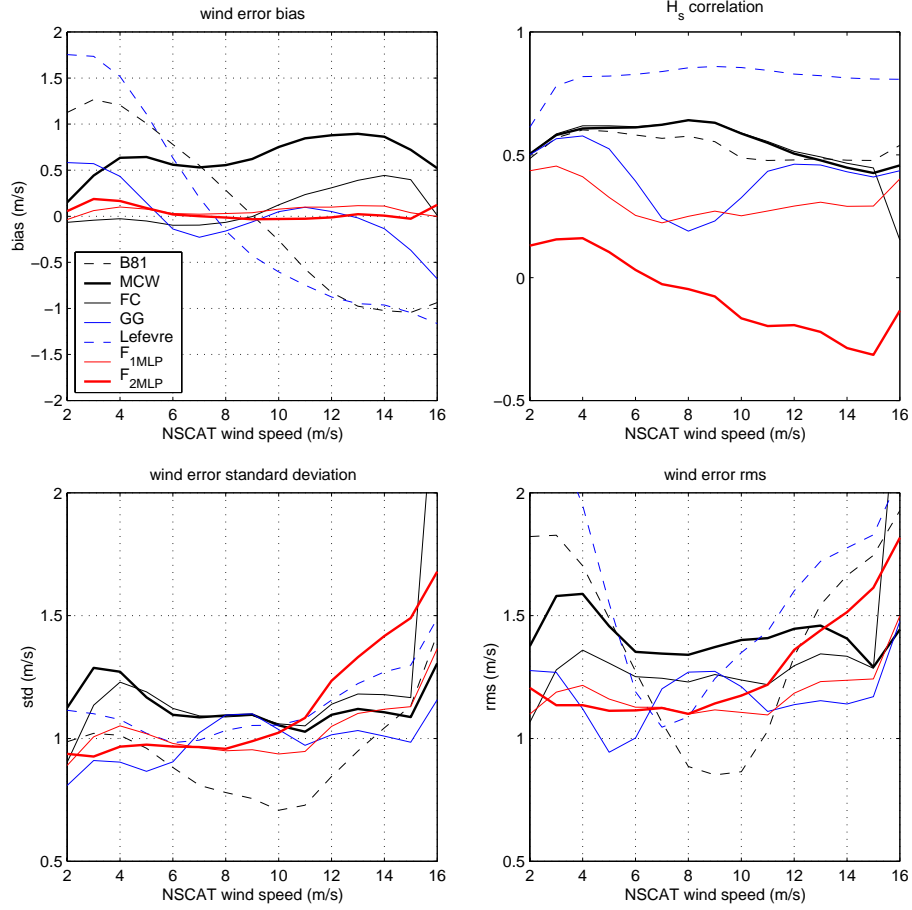


Figure 12: Some statistical characteristics of various altimeter wind speed algorithms as function of NSCAT wind speed : bias, standard deviation, SWH correlation of the wind error and root mean square wind error. The different algorithms are B81 (black dashed), MCW (thick black), FC (thin black), GG2 (red), Lefevre (red dashed),  $F_{1MLP}$  (thin blue),  $F_{2MLP}$  (thick blue)

characteristics. All indications are that B81 is a poor choice for an altimeter model function.

We find that MCW has homogeneous characteristics (bias,rms,SWH error trend) over the wind speed range, but a constant bias of about + 0.5 - 0.6 m/s produces systematic increase of error rms. Such a bias is completely consistent with different observations by several authors (Witter and Chelton (1991), Glazman and Greyzikh (1993), Freilich and Challenor (1994)) and is responsible for the wind error rms of about 1.3 m/s. FC exhibits lower bias as well as stable bias and rms variation over the range of wind speeds. In fact, we conclude that FC is nearly equivalent in all parameters to MCW with its bias removed. For example the wave height correlation for MCW and FC in figure 12 are almost identical.

Perhaps the most notable new observation here is the strong evidence of the correlation between wind error and the altimeter's estimate of SWH for all the single parameter algorithms. The error slope ( and linear regression correlation coefficient) is strongest in the range 4-9 m/s with values of 0.8 – 0.9. The correlation decreases slightly for the lowest and highest wind speeds considered here and reach a minimum value around 13-15 m/s.

The two parameter algorithms do appear to offer consistent performance improvement aside from Lefevre et al. (1994). It is clear that this algorithm is inferior to all routines being assessed here when one considers all the factors. We thus eliminate it from further discussion. Next, one can see from the tables and figure that the GG2 routine does lead to wind errors statistics that often approach the low levels of the neural solutions. But as one can see the bias is somewhat erratic versus wind speed. Perhaps the most notable characteristic of this model is the abrupt lowering of the wave height error trend for moderate wind speeds of 7-9 m/s. Aside from this region the SWH impact (error trend, correlation) is nearly identical as for the single parameter algorithms. This is indeed a feature of the classification scheme used in that algorithm combined with the large data population for wind speeds in this moderate range. In essence, the GG2 leads to a very bimodal wind histogram due to its discontinuous nature (much as for B81).

As alluded to in section three, the SWH error trend for a given wind speed will, by definition, be significantly reduced by our neural models relative to routines such as MCW or FC. Table 4 and Figure 12 clearly indicate that the  $F_{2MLP}$  routine strongly attenuates the SWH error trend (to less than 0.1 m/s/meter while MCW and FC were generally higher than 0.6 m/s per meter SWH). The  $F_{1MLP}$  model provides a reduction but not removal of this trend. Recall from section three that these two algorithms carry different weighting of the wave height due to their alternate training. Both neural solutions provide a very small and stable bias across the complete wind speed range. The rms for the two solutions is nearly identical up to 10 m/s and at that point the  $F_{2MLP}$  begins to increase substantially with increasing wind speed. We have found that this increase is related to the strong multi-valuedness that the neural network encounters when attempting to optimize the  $(U_{10}, SWH) \rightarrow \sigma^\circ$  mapping over moderate to high wind speeds. The network's average solution,  $F_{2MLP}$ , upon inversion to wind speed, actually leads to a negative correlation with SWH at high winds as seen in Table 4.

Considering all algorithms and observations related to their bias, functional continuity and minimization of the rms error it appears that  $F_{1MLP}$  provides the best overall wind model when evaluated against the TOPEX/NSCAT data set. The improvement is on the order of 10-15 % in terms of the global or local reduction in the wind error standard deviation or rms relative to the operational MCW model function. In an absolute sense, the new routine serves to lower the rms by 0.1-0.2 m/s. Improvements are negligible for the high wind speeds above 12-14 m/s.

## 4.2 Model assessments using other wind speed sources

We next turn to independent data sets for further validation of the proposed globally-based wind speed retrieval methods. Description of these data and their sources were provided in section two. Overall, they encompass reference wind speeds from models, scatterometers and buoys. Each data set possesses its own unique collocation properties with respect to intercomparison noise sources. In some cases these differences will be shown to mask much of what we see in the TOPEX/NSCAT data set. Initial algorithm assessments using these data sets indicates that, for the most part, relative differences between algorithms remained consistent with the TOPEX/NSCAT findings described above. Therefore we condense the discussion to primarily a comparison and contrast between three



routines: FC,  $F_{1MLP}$  and  $F_{2MLP}$ . We chose FC here for the reference single parameter routine because it is essentially the operational MCW routine without the apparent 0.5 m/s overall wind speed bias.

#### 4.2.1 A colocated TOPEX/SeaWinds dataset

Figure 13 shows the comparison between altimeter and scatterometer-derived wind speeds using the QuikSCAT (QSCAT) wind speed as the reference. Both the bias and standard deviation are presented for the FC,  $F_{1MLP}$  and  $F_{2MLP}$  routines. Recall that this collocation featured data with time collocation differences of less than 30 minutes. The TOPEX ground swath for the ( $\sigma^0$ , SWH) estimates was 70 km by 2 km and the QSCAT wind vector cell was about  $25km^2$ . The total number of colocated samples for this data set, after filtering, was 87,913.

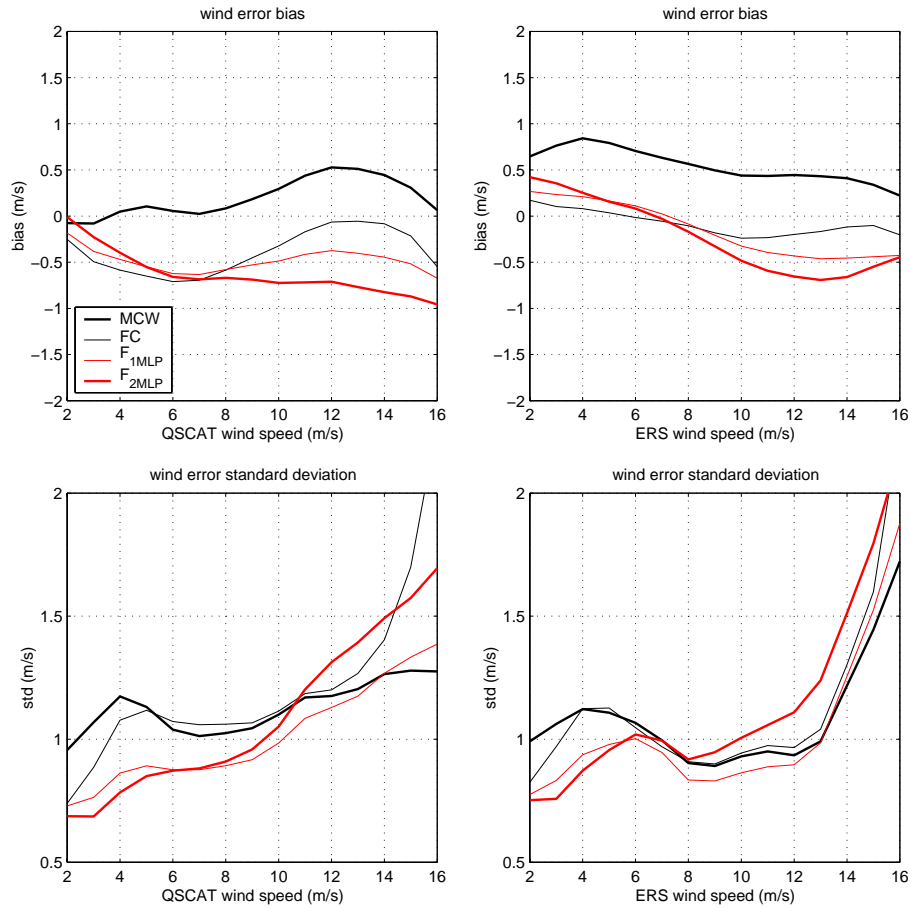


Figure 13: Bias and standard deviation of wind error estimates from various altimeter wind speed algorithms, as function of Seawinds scatterometer (left plot) and ERS-2 scatterometer wind speeds (right plot). The different algorithms are MCW (thick black), FC (thin black),  $F_{1MLP}$  (thin red),  $F_{2MLP}$  (thick red).

Figure 13 indicates that there is some bias change with respect our TOPEX/NSCAT comparison. The MLP solutions are near zero at light winds and then shift to -0.5 to -0.8 for the remaining speeds. FC shows a sinusoidal variation from -0.5 to 0.0. The standard deviation data indicate that

the  $F_{1MLP}$  solution exhibits measureably lower noise levels than for FC. Once again, the  $F_{2MLP}$  rms values match  $F_{1MLP}$  for light-to-moderate winds and then become very high at the higher wind speeds.

Dataset	num. of samples	FC			$F_{1MLP}$			$F_{2MLP}$		
		bias	std	$\alpha_{H_s}$	bias	std	$\alpha_{H_s}$	bias	std	$\alpha_{H_s}$
Topex-NSCAT	48331	0.02	1.16	0.49	0.05	0.99	0.20	0.03	1.03	-0.05
Topex-QSCAT	88324	-0.48	1.18	0.44	-0.53	0.97	0.15	-0.65	1.04	-0.13
Ers-NSCAT	129701	-0.70	1.02	0.47	-0.56	0.87	0.16	-0.48	0.96	-0.08
Topex-ERS	55765	-0.07	1.08	0.27	-0.08	1.01	-0.03	-0.15	1.12	-0.29
Topex-ECMWF1	231102	-0.24	1.84	0.38	-0.20	1.77	0.14	-0.22	1.86	-0.11
Topex-ECMWF2	208518	-0.06	1.64	0.25	-0.05	1.56	0.01	-0.11	1.68	-0.25
Topex-ECMWF3	89188	-0.28	1.60	0.30	-0.30	1.44	0.06	-0.42	1.56	-0.20
Geosat-NDBC	4532	0.24	1.51	0.32	0.39	1.52	-0.04	0.50	1.69	-0.28

Table 5: Wind error bias and standard deviation for  $F_{1MLP}$  and  $F_{2MLP}$  compared to FC, from various datasets described in section 2. The 3 topex-ECMWF estimates come respectively from the 3 datasets topex-NSCAT, topex-ERS and topex-QSCAT. The whole wind speed range 1-17 m/s is considered. Denoting the wind error  $e$ ,  $\alpha_{H_s}$  is defined as the slope in the linear regression  $e = \alpha_{H_s} H_s + \beta$ .

Tables 5 and 6 provide parameters related to  $U_{err}$  similar to those given in Tables 3 and 4. Here the tables summarize the results from the various data sources to be addressed here and below. In these latter tables the TOPEX/NSCAT comparison numbers are derived using colocation samples having a time separation of less than 30 minutes. This makes that variable identical between the TOPEX/NSCAT and TOPEX/QSCAT cases. One can see that for TOPEX/QSCAT the standard deviation is indeed lower for the neural solutions than for FC in all cases with absolute values that are consistent with those seen in the TOPEX/NSCAT comparisons. Here the +/- thirty minutes colocations between altimeter and Ku-band scatterometer show rms levels from 0.8 to 1.3 depending on wind speed and algorithm.

The wind error's wave height dependence and its removal using the neural network models is also consistent between the data sets. The data of Table 6 show small differences in  $\alpha_{H_s}$  that are most likely due to the bias change between data sets. Otherwise, the basic attenuation ( $F_{1MLP}$ ) or removal ( $F_{2MLP}$ ) of the wave height impact holds as for TOPEX/NSCAT. Thus this Ku-band scatterometer data set affirms our findings.

The main observed difference here then is the 0.5 m/s change in bias. Possible explanations for this small change likely reside in TOPEX absolute calibration drift, absolute calibration difference between NSCAT and SeaWinds, and/or the change from NSCAT-1 to NSCAT-2 GMF used to derive the scatterometer wind speeds.

Dataset 3-5 m/s	FC			$F_{1MLP}$			$F_{2MLP}$		
	bias	std	$\alpha_{H_s}$	bias	std	$\alpha_{H_s}$	bias	std	$\alpha_{H_s}$
Topex-NSCAT	-0.03	1.23	0.92	0.10	1.05	0.52	0.16	0.96	0.19
Topex-QSCAT	-0.59	1.07	0.68	-0.47	0.86	0.36	-0.40	0.79	-0.01
Ers-NSCAT	-0.92	0.86	0.53	-0.72	0.76	0.29	-0.51	0.70	-0.10
Topex-ERS	0.08	1.12	0.79	0.21	0.94	0.38	0.25	0.87	0.05
Topex-ECMWF1	-0.01	1.85	0.93	0.13	1.83	0.59	0.20	1.81	0.26
Topex-ECMWF2	0.05	1.63	0.81	0.19	1.57	0.44	0.25	1.53	0.10
Topex-ECMWF3	-0.19	1.42	0.68	-0.05	1.33	0.33	0.02	1.28	-0.02
Geosat-NDBC	0.12	1.40	0.46	0.41	1.40	0.04	0.54	1.39	-0.28
<b>7-9 m/s</b>									
Topex-NSCAT	-0.07	1.09	0.78	0.03	0.95	0.27	-0.01	0.96	-0.05
Topex-QSCAT	-0.59	1.06	0.70	-0.58	0.89	0.15	-0.67	0.91	-0.14
Ers-NSCAT	-0.77	0.89	0.67	-0.53	0.79	0.11	-0.49	0.83	-0.18
Topex-ERS	-0.11	0.91	0.54	-0.09	0.84	-0.03	-0.17	0.93	-0.34
Topex-ECMWF1	-0.34	1.72	0.94	-0.27	1.68	0.47	-0.30	1.73	0.18
Topex-ECMWF2	-0.04	1.52	0.76	-0.01	1.47	0.25	-0.07	1.53	-0.06
Topex-ECMWF3	-0.33	1.38	0.69	-0.36	1.32	0.16	-0.46	1.37	-0.15
Geosat-NDBC	0.07	1.25	0.35	0.22	1.32	-0.23	0.28	1.49	-0.56
<b>11-13 m/s</b>									
Topex-NSCAT	0.31	1.14	0.57	0.10	1.05	0.30	-0.01	1.23	-0.23
Topex-QSCAT	-0.06	1.20	0.52	-0.37	1.13	0.19	-0.71	1.31	-0.32
Ers-NSCAT	-0.29	1.10	0.48	-0.40	1.01	0.18	-0.35	1.27	-0.36
Topex-ERS	-0.20	0.97	0.44	-0.43	0.90	0.12	-0.66	1.11	-0.40
Topex-ECMWF1	-0.39	1.78	0.68	-0.58	1.69	0.45	-0.74	1.93	0.01
Topex-ECMWF2	-0.21	1.52	0.51	-0.47	1.50	0.20	-0.69	1.76	-0.29
Topex-ECMWF3	-0.10	1.63	0.53	-0.46	1.65	0.21	-0.82	1.90	-0.27
Geosat-NDBC	0.83	1.57	0.39	0.59	1.55	0.08	0.66	2.01	-0.45

Table 6: Wind error bias and standard deviation for  $F_{1MLP}$  and  $F_{2MLP}$  compared to FC, from various datasets described in section 2. The 3 topex-ECMWF estimates come respectively from the 3 datasets topex-NSCAT, topex-ERS and topex-QSCAT. Three separate wind speed ranges were considered, 3-5, 7-9 and 11-13 m/s. Denoting the wind error  $e$ ,  $\alpha_{H_s}$  is defined as the slope in the linear regression  $e = \alpha_{H_s} H_s + \beta$ .

#### 4.2.2 A colocated ERS-2/NSCAT dataset

We use the ERS-2 altimeter colocated with NSCAT scatterometer wind speeds to provide an assessment of the algorithms using a completely different altimeter. The ERS-2 wind speed estimate difference from NSCAT are summarized in Tables 5 and 6. Once again one sees a -0.5 to -0.7 bias for the global wind speed regime for all three algorithms shown. The overall standard deviation numbers appear to be somewhat lower than for the upper two data sets in the table.

As with the data assessed above, one finds that the  $F_{1MLP}$  solution exhibits standard deviation levels of the order of 10 % lower than for the FC routine. Table 6 suggests that the relative decrease in SWH error trend is also consistent with our documented expectations.

#### 4.2.3 A colocated TOPEX/ERS dataset

The TOPEX/ERS scatterometer data set provides the chance to assess wave height impacts on wind error when the reference wind speed comes from a C-band scatterometer rather than Ku-band as in the examples above. The ERS scatterometer footprint here is  $50km^2$  and so another difference is the increased spatial size used to derive the wind speeds. The expectation is that this difference will be most evident for light and high wind cases where 50 km approaches the length scale of atmospheric signatures for these regimes.

Figure 13 shows the wind error bias and standard deviation with the ERS wind speed as the reference. The bias for all three test algorithms is near 0.0 at 7 m/s. The bias magnitude stays below 0.2 for FC and 0.4 for  $F_{1MLP}$  (see table 6) but one does see a positive bias at light winds and negative level for high winds. This feature is likely somewhat related to the sampling size and asymmetry in the regression between the two wind parameters (e.g. see section 2 figure 3).

The standard deviation between TOPEX and ERS scatterometer winds is always lowest when using the  $F_{1MLP}$  algorithm when compared to the single parameter FC. Again we see the  $F_{2MLP}$  wind error noise increases with increasing wind speed.

Perhaps most notable here is that the SWH removal is stronger than for Topex-NSCAT : for a similar reduction of wind error's wave height trend (-0.73 to -0.88 for  $F_{2MLP}$ , see table 6), correlation is decreased with Topex-ERS (Topex-NSCAT) by 0.57 (0.47) at 3-5 m/s, 0.91 (0.70) at 7-9 m/s and 0.90 (0.73) at 11-13 m/s (these numbers for Topex-ERS are not reported in any table or figure; for Topex-NSCAT, see figure 12). Figure 14 shows that, referenced to ERS-2 scatterometer, Topex  $\sigma_{Ku}^o$  seems to have lower SWH impact than using NSCAT, QSCAT or ECMWF reference (for a given 3.5 m SWH variation, we get 0.6 dB variation at 8 m/s instead of 0.8 dB). As sampling and time period are similar, and no effect of different Topex time average was observed, such a difference might indicate that C-band ERS wind estimates contain SWH impact. However, the observed 0.2 dB may not be significant as we see a similar lower variation when using ERS-2 altimeter  $\sigma_{Ku}^o$  rather than TOPEX. Thus, we raise this point but claim that within the scope of this study it is not conclusive.

We also notice from table 6 that the  $F_{1MLP}$  wind error std is much higher than for the other scatterometer data sets. This could be explained by the point alluded in the above paragraph. It may also mean that a residual noise level related to space and time samplings is reached, as seems to be the case for ECMWF wind speeds (see next paragraph).

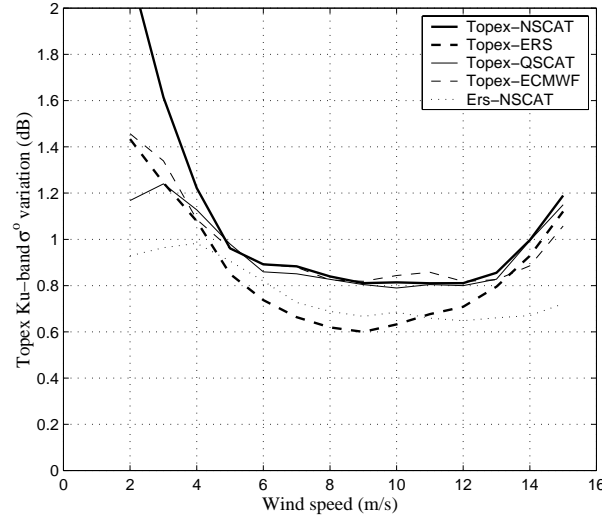


Figure 14: Global Ku-band altimeter  $\sigma^o$  variation associated with a SWH variation of 3.5 m. The specified range is changing with wind speed. Results are presented for 5 different datasets : Topex-NSCAT (thick), Topex-ERS (thick dashed), Topex-QSCAT (thin), Topex-ECMWF (thin dashed) and Ers-NSCAT (dotted).

#### 4.2.4 Colocated TOPEX/ECMWF datasets

Next we are able to compare altimeter-derived winds with interpolated estimates from the ECMWF global surface analysis data sets. As mentioned, we have these data for the three separate scatterometer collocations. We denote these as Topex-ECMWF(1,2,3) as presented in Tables 5 and 6. The main feature of these data sets is the large space and time sampling and collocation differences between the 2 km TOPEX estimate and the one deg. grid model provided every six hours. Thus we expect a substantial impacts in intercomparison noise and bias, especially for the light and high wind speeds. This is in fact what we find.

Figure ECMWF presents the wind error bias and standard deviation for the three test algorithms and the three separate data sets. The bias variations with wind speed are not unlike the TOPEX/ERS results - positive for light winds tending to negative at high winds. The bias for all algorithms is below 0.5 at a wind of 7 m/s. One can see from Table 5 that the overall bias for our three separate ECMWF cases is below 0.3 m/s. Thus we feel that these data show that the algorithm biases are not too substantial.

Regarding the rms, it is clear from Figure ECMWF that the wind error level has increased up to levels of 1.5-1.8, an increase of 30 – 45% over the previous data comparisons. This value is consistent with the increase in intercomparison noise suggested by Dunbar and Freilich (1993) in their comparison of altimeter winds to model winds.

We note that the noise level of the FC and  $F_{1MLP}$  solutions is very nearly identical here. We conclude that the improvement seen in the previous examinations is now masked by the intercomparison noise.

Examination of Table 6 for the ECMWF rows shows that, while rms may not be clearly reduced

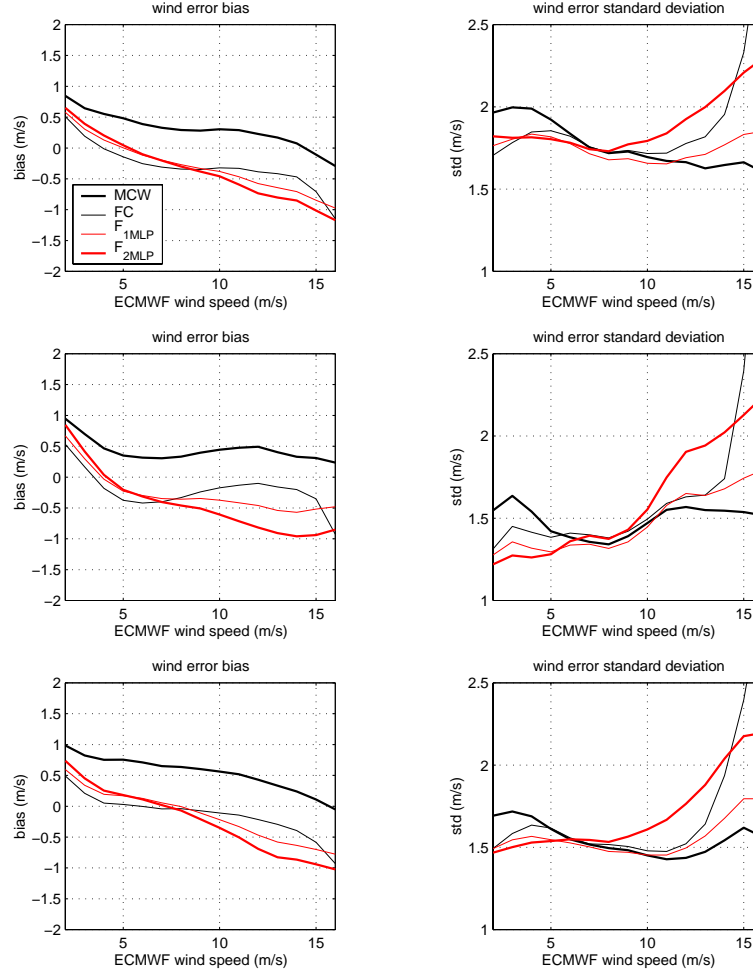


Figure 15: Bias and standard deviation of wind error estimates from various altimeter wind speed algorithms, as function of ECMWF wind speed. Upper plots come from NSCAT-TOPEX dataset, center plots from ERS-TOPEX, and bottom plots from QSCAT-TOPEX. The different algorithms are MCW (thick black), FC (thin black),  $F_{1MLP}$  (thin red),  $F_{2MLP}$  (thick red).

using the MLP routines, the relative reduction of wind error dependence on SWH does occur for these routines. The reduction of this impact is consistent with the scatterometer comparisons.

#### 4.2.5 A colocated Geosat/NDBC buoy dataset

Finally, we also provide altimeter wind results for the Geosat/NDBC dataset previously used by Glazman and Greysukh (1993) and Freilich and Challenor (1994). The bias for all algorithms is below 0.5 m/s. As for ECMWF observations in the preceding paragraph, the noise level of the FC and  $F_{1MLP}$  are very close (1.50 m/s) and any improvement is hidden behind the intercomparison noise. This might also mean that our global neural models are not well-suited to be used regionally in the NDBC area. Still, though there is no measurable rms improvement, table 6 does indicate that the wind error dependence on SWH is reduced when using both  $F_{1MLP}$  and  $F_{2MLP}$ . The reduction

is quite consistent with observations from the other datasets.

### 4.3 Conclusion

In the preceding section, we have shown that our neural network-derived models are independent on the dataset used to train it. This is a further assessment of their validity. As discussed in the past by Freilich and Challenor, Glazman and Greysukh, a required characteristic of any wind speed algorithm should be to well reproduce the global wind statistics; we have shown in section 3 (see figure 8) that our models do have this characteristics, particularly the MLP ones. In addition, we showed that  $F_{1MLP}$  nicely matches the global reference wind speed, taking into account most of its characteristics.

Considering that wind estimate error is significantly improved, we suggest to use  $F_{1MLP}$  as an operational altimeter wind speed retrieval algorithm. Up to 10-12 m/s, it produces a significant improvement of wind error rms. For higher wind speeds, it does not produce better estimate than any single parameter algorithm.

In section 5, we will describe the C-band measurements simultaneous to the TOPEX Ku-band ones, expecting some higher sea state correlation.

## 5 C-band altimeter models and validation

This section documents functions relating TOPEX C-band altimeter backscatter coefficient,  $\sigma_C^o$ , to near-surface wind speed and significant wave height. The basis for these functions will once again be the combined TOPEX/NSCAT data set (section 2) and use of neural network techniques.

The basic physical model for radar backscatter at near-vertical incidence is one of quasi- specular reflection - increase in the overall surface roughness leads to decrease in the radar backscatter. Chapron et al. (1996) discuss TOPEX C and Ku-band observations and the physical expectation that a C-band altimeter should be less responsive to surface wind speed changes than a Ku-band radar because of the differing probing wavelengths (5 cm for C-band versus 2 cm for Ku-band). The ocean surface slope variance is thought to relate well to the altimeter backscatter and it is well documented that the largest contributions to the total slope variance come from ocean length scales below 10 cm. An informed Geometric Optics approximation suggests that the altimeter senses reflection from wave scales with horizontal extent of three times the radiated wavelength - this is the so-called filtered surface response. Summation of these details leads to the notion that C and Ku-band altimeters should provide nearly identical backscatter response from those waves of length greater than 15 cm. A Ku-band altimeter's increased sensitivity to winds must come from its increased sensitivity to the waves shorter than 10-15 cm. Conversely, because the C-band system likely carries less wind information in its backscatter it should contain relatively more information related to long-wave impacts. So in this section dealing strictly with the C-band altimeter responses one can assume a degraded response in comparison to the wind speed results of section 4 but perhaps a higher correlation with the altimeter significant wave height estimates.

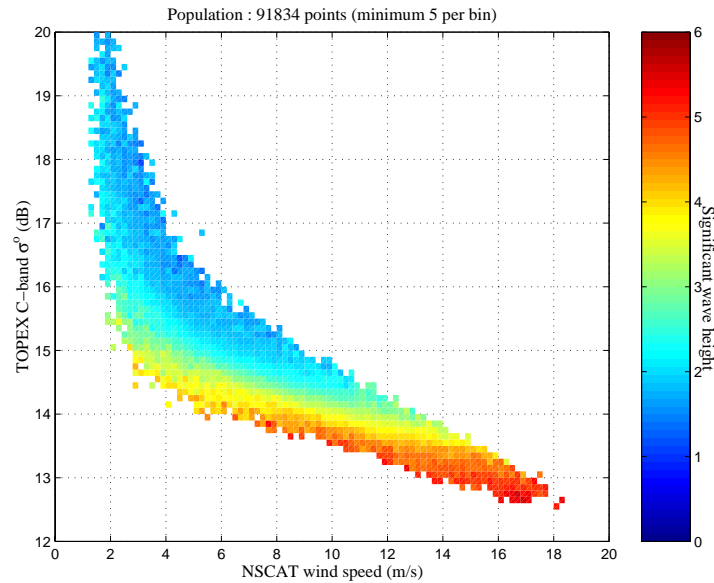


Figure 16: Gridding of averaged TOPEX  $\sigma_C^o$  versus NSCAT wind speed. Color variation represents corresponding SWH values.

Figure 16 shows the overall relation of the C-band backscatter to the 10 m surface wind speed of NSCAT and to the altimeter wave height estimate. These data come from the same colocated data



set as used in section 3. The time ( $\pm 1$  hour) and spatial colocation ( $< 12$  km) are the same. The color of pixels within the grid once again represent the average value of the significant wave height at that point on the  $(\sigma_C^\circ, U_{10})$  grid. Referring to Fig 4 one can see strong similarity between C and Ku-band altimeter responses to both wind speed and to SWH. The C-band signal is on average about 3 dB above the Ku-band which is partially explained by the frequency- dependent dielectric constants and absolute calibration error. The C-band backscatter exhibits the same two regime character as the Ku-band versus wind speed where the signal rises dramatically at the light wind speeds. One small but fundamental difference between the two frequency responses is the flatness of  $\sigma_C^\circ$  with respect to wind changes above 10 m/s.

We provide Figure 17a to directly compare the C and Ku-band observations. This figure shows that the correlation between wind error and wave height is generally within 5-10 difference increases greatly above 10-12 m/s. Note the the mention of  $F_{3MLP}$  refers to an algorithm described in the following section. The second panel on Figure 17 provides an isolation of the behavior for both backscatter signals (C and Ku-band) for the NSCAT wind speed of 7 m/s. The caption indicates the higher correlation with wave height for C-band.

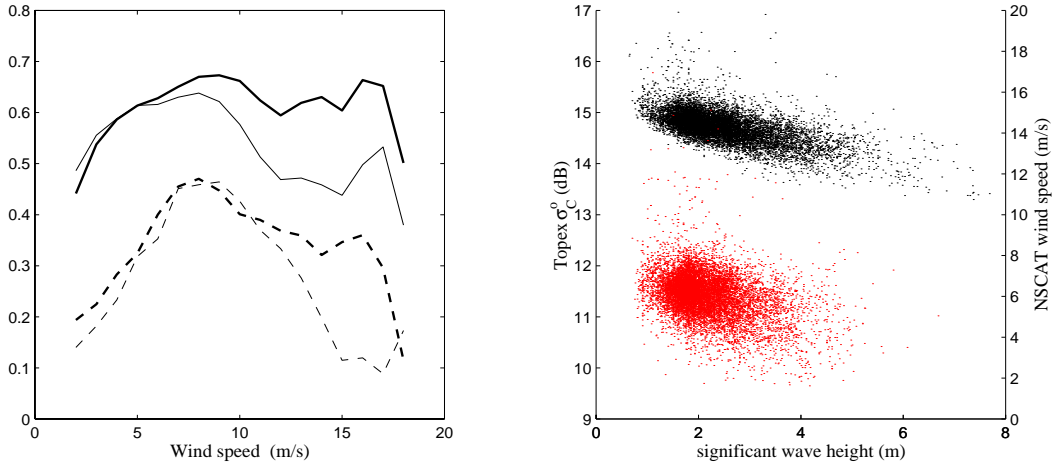


Figure 17: Left panel : correlation of the wind speed error  $U_{mcw} - U_{nscat}$  (thin) and  $U_{altF3} - U_{nscat}$  (thick) distribution with SWH. Full lines are for constant  $U_{nscat}$ , dashed lines are for constant  $\sigma_{Ku}^\circ$  [i.e. constant equivalent  $U_{mcw}(U_{altF3})$ ]. Right panel :  $\sigma_C^\circ$  as function of SWH for  $U_{nscat} = 7 \pm 0.5$  m/s (black dots) with linear regression correlation coefficient  $-0.56$ ;  $U_{nscat}$  as function of SWH for  $\sigma_C^\circ = 15 \pm 0.15$  dB (red dots) with correlation  $-0.36$ .

## 5.1 Model developments

Previous authors (e.g. Chapron et al., 1996; Quartly et al., 1997; Elfouhaily et al., 1998) have discussed the response of C-band backscatter to wind speed via direct comparison or in tandem with the Ku-band backscatter of TOPEX. We develop stand-alone C-band model functions in this section to document and validate the TOPEX C-band system using completely independent wind speed information. We choose to develop these functions using the non-parametric neural network solutions to encompass the dynamics of the nonlinear relationships shown in figure 16. For completeness, we will provide single parameter (analogous to the operational Ku-band MCW algorithm) and dual

parameter solutions - as developed in section three for the Ku-band system.

### 5.1.1 C-band backscatter versus wind speed

We define the single parameter mapping between  $\sigma_C^\circ$  and NSCAT wind speed as :

$$U_{10} = F_3(\sigma_C^\circ) \quad (9)$$

and generate the MLP neural network solution over this two dimensional data space in the same manner and for the same TOPEX/NSCAT data as described in sections 2 and 3. The only differences being that here we are dealing with  $\sigma_C^\circ$  and are not including the third (wave height) parameter. Figure 18 shows the resulting relationship. In this case the mapping is quite continuous and could likely be well-approximated over most of wind speed range using a polynomial. Our neural network solution is defined in annexe B.

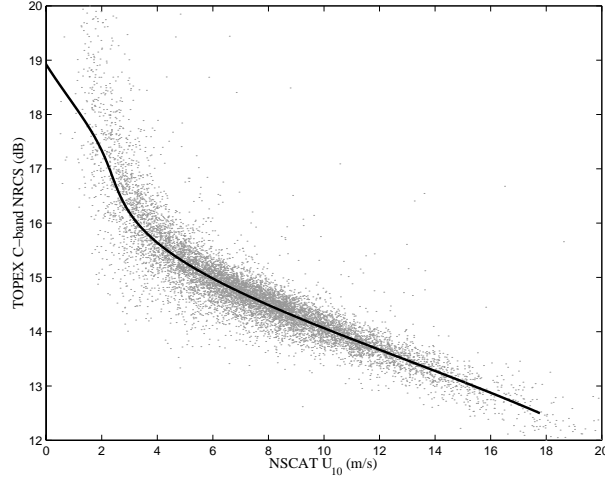


Figure 18: Scatter plot of TOPEX C-band  $\sigma^\circ$  as function of wind speed. Only 10 % of the dataset were represented. Thick line corresponds to our  $F_3$  model.

Table 7 provides the resulting validation information in terms of the C-band wind speed error where the C-band wind speed,  $U_{altC}$ , is derived directly from  $F_3$  :

$$U_{errF3} = U_{altC} - U_{10} \quad (10)$$

As shown in table 7,  $U_{altC}$  has been compared with several different wind products, a subset of those discussed in validating the Ku-band wind speeds in section four. We find an overall low bias, tending to slightly decrease with wind speed.  $F_{3MLP}$ 's standard deviation is about 8% higher than the Ku-band FC algorithm.

For each wind speed regime - 4, 8 and 12 m/s,  $\alpha_{H_s}^{F_3}$  is greater than  $\alpha_{H_s}^{FC}$ . This indicates the C-band nadir backscatter contains more SWH information than Ku-band. This effect increases with increasing wind speed. This SWH impact perturbates a single parameter wind speed retrieval, and

	Topex-NSCAT			Topex-ERS			Topex-ECMWF		
<b>1-17 m/s</b>	bias	std	$\alpha_{H_s}$	bias	std	$\alpha_{H_s}$	bias	std	$\alpha_{H_s}$
FC	0.02	1.16	0.49	-0.07	1.08	0.27	-0.20	1.82	0.35
$F_3$	0.01	1.25	0.48	0.12	1.27	0.27	-0.19	1.81	0.42
$F_1$	0.05	0.99	0.20	-0.08	1.01	-0.03	-0.14	1.73	0.14
$F_2$	0.03	1.03	-0.05	-0.15	1.12	-0.29	-0.16	1.81	-0.10
$F_4$	0.03	1.12	0.31	0.12	1.19	0.11	-0.17	1.77	0.24
$F_5$	0.04	1.17	-0.03	0.10	1.30	-0.22	-0.15	1.90	-0.09
<b>3-5 m/s</b>									
FC	-0.03	1.23	0.92	0.08	1.12	0.79	0.00	1.82	0.97
$F_3$	0.17	1.36	0.99	0.42	1.28	0.89	0.04	2.05	1.06
$F_1$	0.10	1.05	0.52	0.21	0.94	0.38	0.16	1.82	0.62
$F_2$	0.16	0.96	0.19	0.25	0.87	0.05	0.24	1.79	0.30
$F_4$	0.17	1.21	0.61	0.42	1.13	0.51	0.11	1.89	0.69
$F_5$	0.25	1.18	0.16	0.50	1.07	0.04	0.17	2.01	0.29
<b>7-9 m/s</b>									
FC	-0.07	1.09	0.78	-0.11	0.91	0.54	-0.32	1.69	0.96
$F_3$	0.00	1.12	0.83	0.21	1.05	0.62	-0.23	1.63	0.99
$F_1$	0.03	0.95	0.27	-0.09	0.84	-0.03	-0.24	1.63	0.49
$F_2$	-0.01	0.96	-0.05	-0.17	0.93	-0.34	-0.27	1.68	0.20
$F_4$	-0.02	1.04	0.52	0.16	1.01	0.28	-0.25	1.64	0.70
$F_5$	0.07	1.07	-0.03	0.21	1.14	-0.31	-0.16	1.73	0.19
<b>11-13 m/s</b>									
FC	0.31	1.14	0.57	-0.20	0.97	0.44	-0.31	1.79	0.47
$F_3$	-0.02	1.20	0.73	-0.31	1.12	0.65	-0.47	1.63	0.89
$F_1$	0.10	1.05	0.30	-0.43	0.90	0.12	-0.46	1.66	0.45
$F_2$	-0.01	1.23	-0.23	-0.66	1.11	-0.40	-0.64	1.90	0.01
$F_4$	0.06	1.18	0.45	-0.28	1.06	0.35	-0.47	1.71	0.63
$F_5$	-0.07	1.29	-0.15	-0.47	1.20	-0.27	-0.66	1.88	0.09

Table 7: Wind error bias and standard deviation for the five neural algorithms compared to FC, from three datasets described in section 2, topex-NSCAT, topex-ERS and topex-ECMWF. Upper part concerns the whole 1-17 m/s wind speed range; the following focuses on three separate wind speed ranges, 3-5, 7-9 and 11-13 m/s. Denoting the wind error  $e$ ,  $\alpha_{H_s}$  is defined as the slope in the linear regression  $e = \alpha_{H_s} H_s + \beta$ .

thus, it is not surprising to see that  $F_3$  has higher wind error noise than FC. Standard deviation difference is relatively low at 7-9 m/s, and higher at 3-5 and 11-13 m/s. Overall, the C-band system appears to relieve wind speed almost as well as Ku-band, but its higher SWH impact (higher trends) is responsible for the slightly higher global error.

As for Ku-band, the TOPEX-ERS dataset indicates a tendency for positive (negative) bias at low

(high) winds, and minimal bias at 8 m/s. For most wind speeds, the rms is slightly lower by 5 – 10% when compared to TOPEX-NSCAT data. The exception being for wind speeds above 13 m/s. TOPEX-ECMWF data show similar bias evolution with wind speed, and the standard deviation is systematically higher by 0.5 m/s than for TOPEX-NSCAT (or TOPEX/ERS) because of the increased intercomparison noise.

### 5.1.2 Two models for C-band backscatter versus wind speed and wave height

Here two MLP neural network solutions are developed in precisely the same manner as for  $\sigma_{Ku}^o$  in section three where the neural is developed to map two known inputs to one known output. As in that section, we define two functions, swapping the place of wind speed and altimeter backscatter between input and output in the neural training:

$$U_{10} = F_4(\sigma_C^o, SWH) \quad (11)$$

$$\sigma_C^o = F_5(U_{10}, SWH) \quad (12)$$

The difference between these two solutions remains the same as discussed in section three. Physically, we expect to find a measurably higher correlation between SWH and  $\sigma_C^o$  than between SWH and  $U_{10}$  and as observed figure 17a. Thus the function leading to the best characterization of the average wave height response as seen in figure 16 should be  $F_4$ . To get some quantitative idea we compute the correlation coefficient between these parameters in a binned region for a moderate wind speed,  $7 \pm 0.5 \text{ m/s}$  for wind speed and  $15 \pm 0.15 \text{ dB}$  for C-band backscatter. Data are shown in figure 17b. The linear regression correlation coefficient  $R_{F_4}(SWH, \sigma_C^o) = -0.56$  and  $R_{F_5}(SWH, U_{10}) = -0.36$ .

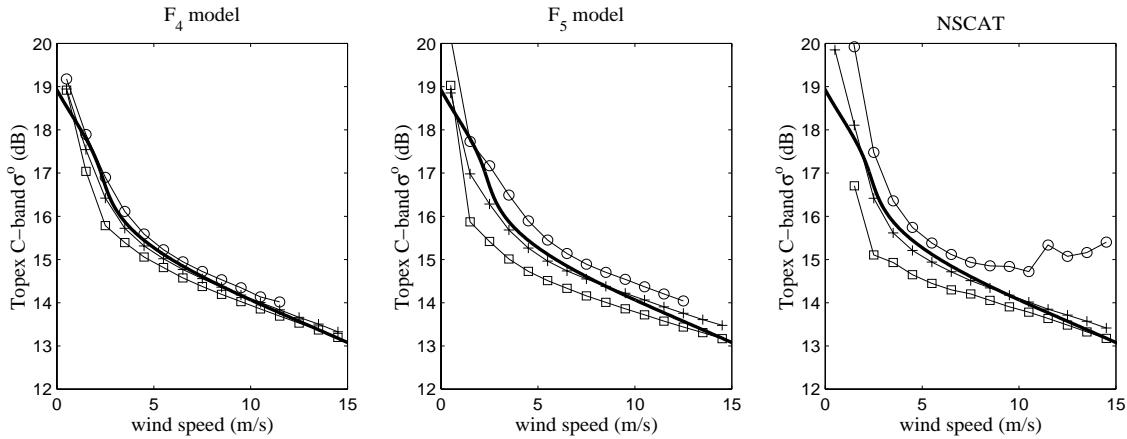


Figure 19: Average behaviour of the  $F_4$  and  $F_5$  neural models for different SWH classes : 1m (circles), 3m (pluses) and 5m (squares).  $F_3$  model is represented for comparison (thick line). The third panel provides averaging of the observed data as for figure 16

Figure 19 shows the overall characteristics of the two neural network solutions  $F_4$  and  $F_5$  along with the actual averaged backscatter observations at these wave heights. Our solutions  $F_4$  and  $F_5$

are described in annexe B. The similarities to the Ku-band solutions ( $F_1$  and  $F_2$ ) of section three are obvious. To obtain a wind speed estimate using  $F_5$ , the model should be run on a regular grid and then inverted.

Table 7 provides the resulting validation information in terms of the C-band wind speed error where the C-band wind speeds,  $U_{altF4}$  and  $U_{altF5}$ , are derived directly from  $F_5$  and from inversion of  $F_5$  :

$$U_{errF4} = U_{altF4} - U_{10} \quad (13)$$

$$U_{errF5} = U_{altF5} - U_{10} \quad (14)$$

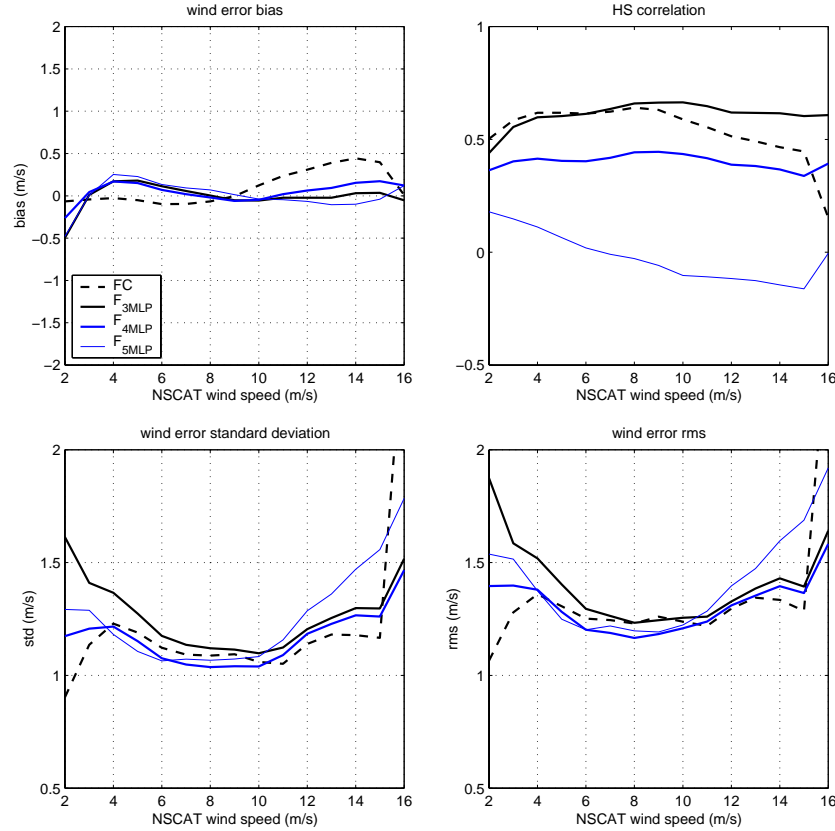


Figure 20: Wind error bias, standard deviation, rms and  $H_s$  correlation for the C-band neural algorithms  $F_{3MLP}$ ,  $F_{4MLP}$  and  $F_{5MLP}$ . Data from the topex-NSCAT dataset were used.

As shown,  $U_{altF4,5}$  are compared with several different wind products, a subset of those discussed in validating the Ku-band wind speeds in section four. We find biases of same order as for FC,  $F_3$  and Ku-band  $F_1$  and  $F_2$  comparison algorithms.

One observes a similar differentiation between  $F_4$  and  $F_5$  as for the Ku-band  $F_1$  and  $F_2$  in that the former 'forward mapping' routines attenuate, rather than remove, the wave height dependence. This is illustrated in Figure 21 showing backscatter variation for both frequency band algorithms and observations versus the NSCAT wind speed. The main observation here is the the variation

permitted under the  $F_4$  is much lower. Also, note the amplitude of SWH impact on  $\sigma^\circ$  measured in decibels is nearly identical between C-band and Ku-band for any wind speed.

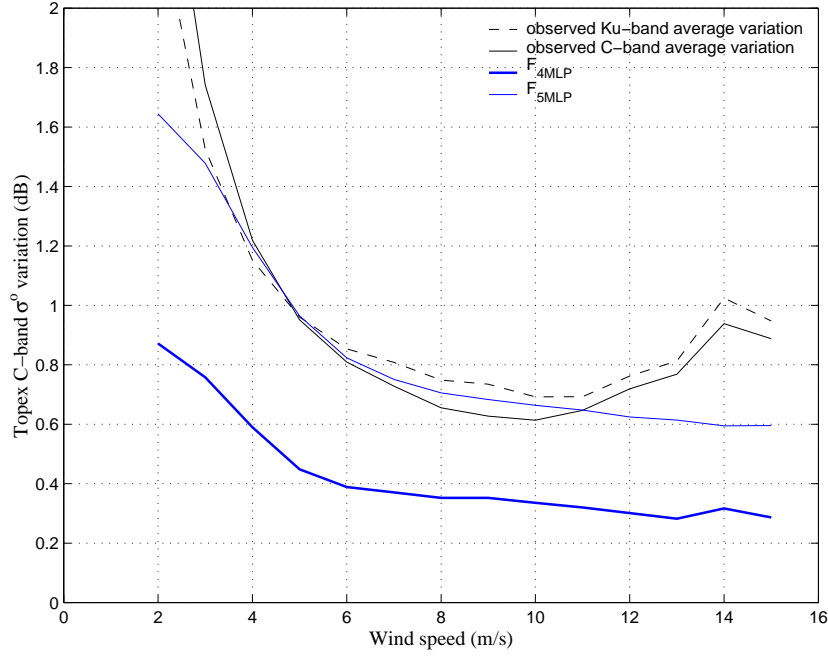


Figure 21: Global TOPEX  $\sigma^\circ$  variation associated with a SWH variations of 3.5 m in extent. This SWH range of variation changes with wind speed. Black full (dashed) line concerns observed C-band (Ku-band) variation versus NSCAT wind speed. Blue lines represent C-band variation as function of  $F_{4MLP}$  (thick) and  $F_{5MLP}$  (thin).

Referring to the figures and Table 7 it is apparent that  $\alpha_{H_s}$  is systematically reduced by integration of SWH information, but  $F_4$  appears to be less efficient than the Ku-band equivalent,  $F_1$ , especially at 8 and 12 m/s. This should be related to the higher ( $\sigma^\circ$ , SWH) correlation for C-band at those wind speeds (see figure 17a) that raises  $F_4$  noise level above  $F_1$ .

At 4 and 8 m/s,  $F_5$  is able to remove SWH impact as well as for the Ku-band  $F_2$ . Again, this can be anticipated from the observations in figure 17a where  $(U_{10}, \text{SWH})$  correlations at a given  $\sigma_C^\circ$  or  $\sigma_{Ku}^\circ$  differ only above 11 m/s. Thus, above 11 m/s, it is not surprising that  $F_5$  is less efficient than  $F_2$ .

Finally figure 20 presents wind error bias, std, rms and SWH correlation for our 3 C-band ( $F_3$ ,  $F_4$  and  $F_5$ ) models, and FC for comparison. The three algorithms have very low bias ( $< 0.25$  m/s for any wind speed) and quite low rms values.  $F_3$  reproduces FC characteristics well, indicating only slightly higher error.  $F_4$  and  $F_5$  provide slight error improvement in comparison to FC by about 5% up to 10 m/s.

## 5.2 Conclusion

Wind estimates using the TOPEX C-band altimeter  $\sigma^\circ$  indicate an ability to nearly match the Ku-band sensor's accuracy for wind speeds below 10 m/s, but the rms is measurably worse than for Ku-

band at higher winds. This would suggest a saturation effect in the C-band backscatter with respect to the short wind waves. Inclusion of sea state impacts via the altimeter's SWH parameter reduces C-band wind error by 5 – 10%. C-band and Ku-band  $\sigma^o$  have similar signatures for SWH impacts for wind speeds up to 8-10 m/s. Above this wind level C-band correlation with SWH substantially exceeds that for the Ku-band. We expect that the differences seen here will become amplified for the ENVISAT altimeter where a Ku and S-band combination will be employed.

## 6 Recommended operational algorithm

This section is devoted to presentation of a recommended neural network solution  $F_{1MLP}$  for use in operational Ku-band altimeter wind speed retrieval. This proposed geophysical model function (GMF) directly computes a 10 m wind speed from altimeter measurements of  $\sigma^\circ$  and SWH. This GMF, developed using TOPEX, is a smoothly varying function of  $\sigma^\circ$  and SWH as shown in Figure 22. It is apparent that overall functional form between backscatter and wind speed resembles the present operational MCW algorithm. The new routine's inclusion of wave height is depicted for three different wave heights in the figure giving the general sense of the 0.5 dB (or  $\pm 1.5$  m/s) deviations from MCW that will now occur to attenuate sea state errors. We note that form of the algorithm is such that it should be easily adjusted for Ku-band  $\sigma^\circ$  absolute calibration adjustments.

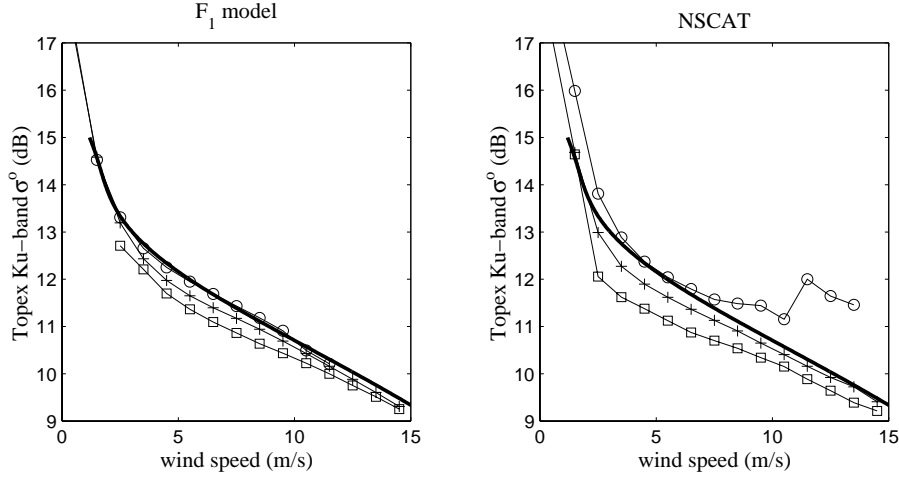


Figure 22: Right panel represents the averaged data used for  $F_{1GRNN}$  ( $F_{2GRNN}$ ) training. Left panel : average behavior of the  $F_{1MLP}$  neural model for three selected SWH classes : 1m (circles), 3m (pluses) and 5m (squares). Right panel represents the averaged data using NSCAT reference wind speed. MCW model is represented for comparison (thick line) on both panels.

$F_{1MLP}$  is defined in Annexe A.

Figure 23 shows that  $F_{1MLP}$  model function has a smooth histogram. This is a required characteristic of an operational algorithm, especially for use in climatological studies as mentioned by Glazman and Greysukh (1993) and Freilich and Challenor (1994).

The objective of this study was to remove or attenuate the systematic trend observed between  $\sigma^\circ$  and SWH at any given wind speed. Figure 24 illustrates the level of success achieved using  $F_{1MLP}$ . We present the average altimeter estimate against the reference NSCAT wind speed about three different SWH values : 1, 3 and 5 m. The SWH range was set to  $\pm 0.5$  m/s.

Finally, figure 25 presents the improvement over the MCW routine obtained using this  $F_{1MLP}$  model function in terms of bias, standard deviation, rms and SWH correlation reduction. These parameters computed over samples within the TOPEX/NSCAT colocation data set. Quantitative measures were also given in sections three and four. We find that the  $F_{1MLP}$  solution has low and invariant overall bias and always reduces the rms (and standard deviation) aside from winds higher than 13



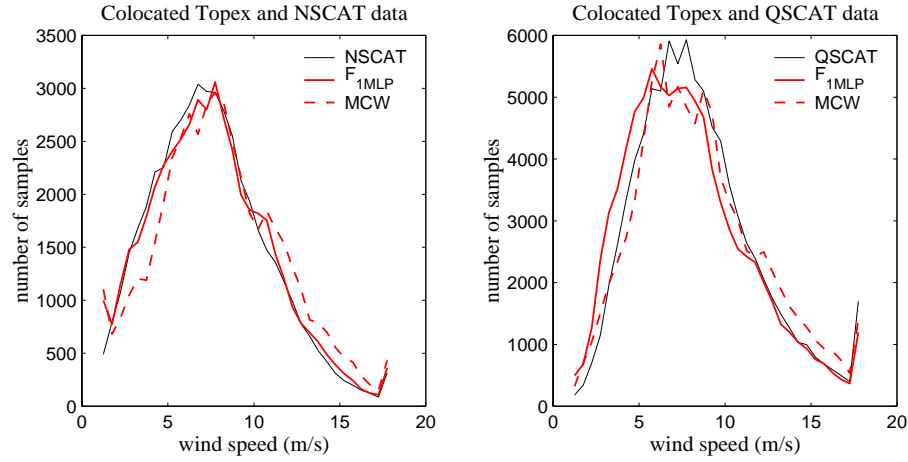


Figure 23: Histograms of three wind speed estimates from scatterometer (black line), altimeter Modified Chelton and Wentz (1991) (red dashed) and  $F_{1MLP}$  (red full). Left plot corresponds to topex-NSCAT colocated dataset, right plot to topex-QSCAT dataset.

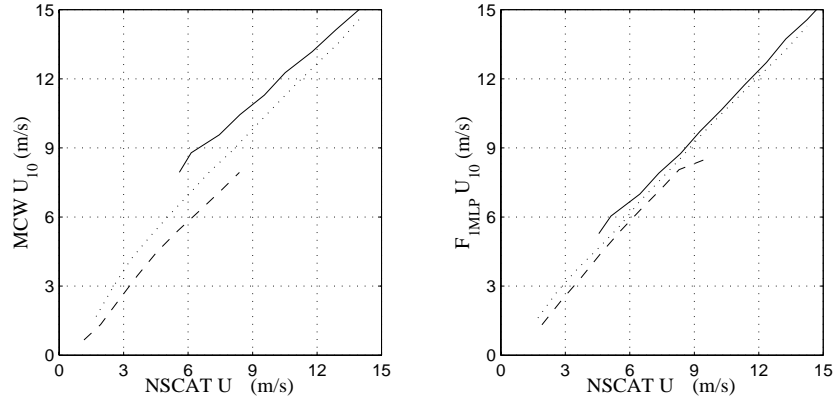


Figure 24: Average relations between  $U_{alt}$  versus NSCAT  $U_{10}$  for different SWH classes : 1m (dashed line), 3m (dotted line), 5m (solid line). SWH range is  $\pm 0.5$  m/s around the indicated value.  $U_{alt}$  is computed from Modified Chelton and Wentz (1991) (left plot) and  $F_{1MLP}$  (right plot).

m/s. The general level of rms reduction from this figure and section four is on the order of 10-15 %.

This routine was developed for wind speeds ranging from 1 - 20 m/s and this should be considered its range of validity. As already noted, the function was developed using TOPEX over the NSCAT operational period of 1996-1997 and using the NSCAT-1 model function. Questions of calibration offsets for the algorithm should thus be referred to this time period and scatterometer GMF. Some issues related to specific (e.g. fetch-limited) applications of this generalized model will be discussed in our closing discussion section.

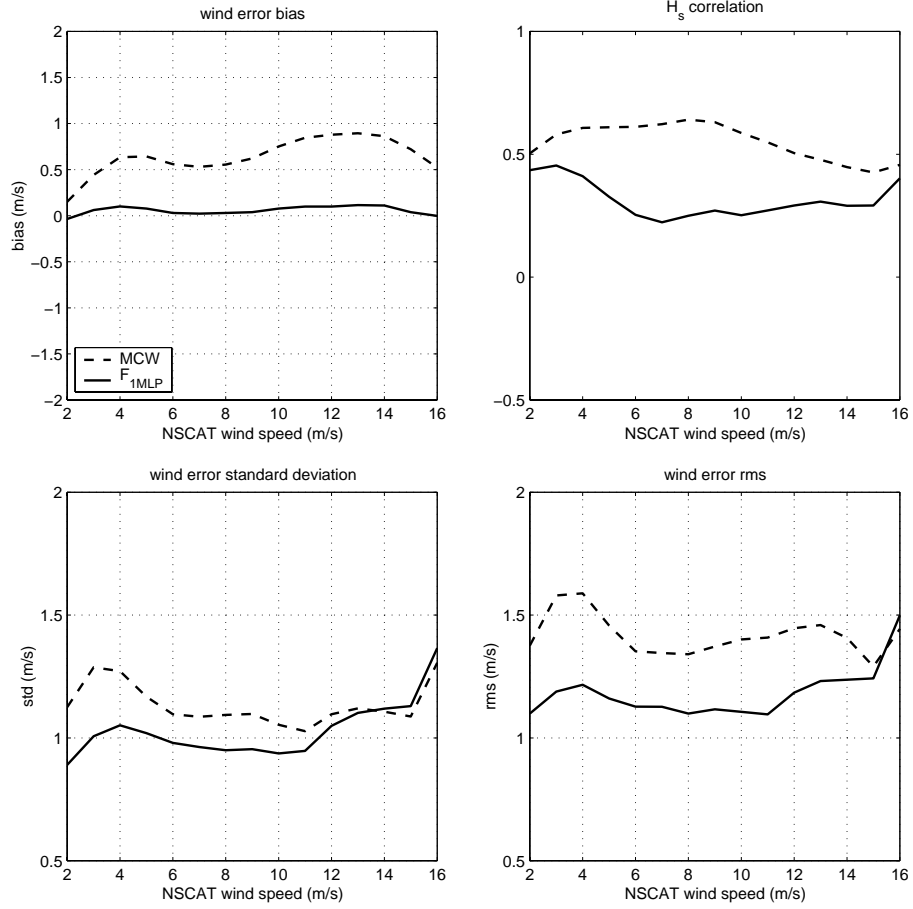


Figure 25: Bias, standard deviation, SWH correlation of the wind error and root mean square wind error from Modified Chelton and Wentz (1991) (dashed line) and  $F_{1MLP}$  (full line) wind speed algorithms. Data used for these plots come from our Topex-NSCAT dataset with a time lag of  $\pm 30$  minutes and a maximum distance between ground tracks of 15 kms.

## 7 Discussion

This report documents the global relationship between near-surface wind speed and TOPEX altimeter measurements of radar backscatter and significant wave height. Models at C and Ku-band have been detailed. The emphasis here has been on global and empirical solutions because the large TOPEX/NSCAT crossover data set permits such an operationally-directed objective. More physically-based evaluation of these data as they relate to air-sea interaction studies are in progress and will be reported elsewhere. In addition, we envision that a multi-year and very large TOPEX/-JASON/SeaWinds crossover data set will permit further refinement of the model functions provided here. This data set should provide more stable representation of sparsely populated backscatter, SWH pairings (e.g. the short-fetch coastal case where high wind combined with low wave height) within our present data set. It will also lead to better accounting for remaining seasonal and regional systematic biases as discussed below.

One fundamental conclusion is that the addition of SWH into the altimeter wind inversion does provide slight but measurable improvement in GMF accuracy. A second conclusion is that these globally-developed two parameter altimeter model functions can not correctly compensate for the long-wave impact on the point-to-point altimeter wind estimates. In fact, the more physically-relevant models developed here for radar backscatter (Ku-band  $F_{2MLP}$  and C-band  $F_{5MLP}$ ) lead to worse performance in wind inversion even though their removal of the average sea state impact was almost complete.

Two basic issues seem to encompass the limitations to use of SWH in routine altimeter wind error corrections. First, any given couplet of radar backscatter and SWH can map to numerous possible surface wind speeds. This ambiguity or multi-valued property is a simple reflection of the fact that SWH is a poor surrogate for variability in long wave conditions (and the impact of those long waves on short waves). Such ambiguity defies development of more accurate point-to-point wind corrections in the absence of more ancillary information.

The second, and perhaps related, issue is our observation that there is an apparent regional signature to the altimeter wind speed error immediately evident in comparison between tropical and high-latitude observations. This latter problem points out one limitation of a single global altimeter wind algorithm and suggests that some regional characterization of error needs to be anticipated. We end the report with brief overview of this issue.

**Regional error in scatterometer and altimeter wind speed** It is well known that the Southern Ocean has a unique wind and wave climatology associated with the geography of the Southern hemisphere. High latitude winds and waves are in general much more energetic and variable than for the mid-latitudes and tropics. This ocean surface wave variability appears to translate to systematic regional biases in altimeter wind speed measurements even after accounting for the average SWH impact through the neural methods developed in this report. The following discussion points out that this may be the case for the C-band scatterometer as well as the Ku-band altimeter.

We recall the various wind products carried in the three datasets TOPEX-NSCAT, TOPEX-QSCAT

	$\delta U_{scat}$	$\delta U_{ecmwf}$	$\delta U_{alt}$	$\delta U_{scat} - \delta U_{ecmwf}$	$\delta U_{alt} - \delta U_{scat}$
Topex-NSCAT	2.0	2.5	3.6	-0.5 (-0.6)	1.6 (0.9)
Topex-QSCAT	2.6	3.6	3.8	-1.0 (-0.6)	1.2 (0.5)
Topex-ERS	3.8	3.0	3.9	0.8 (0.6)	0.1 (-0.1)
Ers-NSCAT	2.2	-	3.2	-	1.0 (0.4)

Table 8: Regional variations of scatterometer, ECMWF and altimeter wind speed estimates. A very crude criterion for regionality was used, that is  $|\phi| < 30^\circ$  (area 1) or  $|\phi| > 45^\circ$  (area 2). First three columns give the observed shift in the histogram of each estimate moving from A1 to A2. Column 4 reports the difference of shift between scatterometer and ECMWF (column 1-2). Column 5 reports the difference of shift between altimeter and scatterometer (column 3-1). Values in parenthesis correspond to SWH restricted to the range  $2.5 \pm 0.5$  m/s.

and TOPEX-ERS described in section 2. All have scatterometer, altimeter and ECMWF wind speed estimates. The ERS-NSCAT data are also included for completeness. For this demonstration the globe is simply divided into two regions with a latitude criterion ( $|\phi| < 30^\circ$ ,  $|\phi| > 45^\circ$ ). Table 8 provides computation of the measured shift towards higher wind speed in the respective wind speed histograms when comparing the low latitude to high latitude area. This shift was computed as the highest coherence lag between two histograms, and does not take into account any histogram shape modification.

The first three columns of Table 8 give the observed shift in the scatterometer, ECMWF and altimeter winds, respectively. One sees fairly consistent results between the different datasets but some clear differences between the varying data source types. Ku-band scatterometers indicate a 2 m/s shift toward higher wind speeds. The Ku-band altimeters and C-band scatterometer (ERS of TOPEX-ERS) show a stronger modification of about 3.5 m/s. The ECMWF shift has an intermediate value of 2.5-3 m/s.

The fourth column represents the difference between the scatterometer wind shift and the ECMWF wind shift; essentially the difference between first and second columns. We observe that Ku-band NSCAT and Seawinds scatterometers indicate a negative shift with respect to ECMWF in comparison to the 0.8 m/s positive bias of the C-band ERS scatterometer. To confirm that such scatterometer observations are not caused by a shift in the average SWH, we also provide the values obtained by averaging data only for the case of SWH within the range  $2.5 \pm 0.5$  m/s. This filtering should insure that any sea state modification is then mainly related to slope/period modifications rather than the overall energy. The value of 2.5 m was chosen in order to obtain a significant amount of data for both areas. Table 8 suggests this filtering does not appear to be too necessary as the table variations are analogous to those obtained from average over all SWH values.

Regarding the scatterometers then, it appears that C-band and Ku-band scatterometers may be impacted differently depending on the wind/wave climate. The C-band instrument seems to over-estimate wind speeds in comparison to Ku-band estimates. It is worth noting that this possible bias is likely to be propagated to ECMWF winds because of the routine assimilation of ERS data

into the ECMWF meteorological model. Neither NSCAT nor QSCAT wind vectors have been assimilated in ECMWF. More work is then certainly suggested to sort out wave climate impacts on scatterometer-retrieved wind speed, but undoubtedly, C-band and Ku-band satellite measurements have a different sensitivity to wind/wave generated surface roughness.

We next address the Ku-band altimeter and its variation. We rely on the preliminary results above and our observations of section 4 where it appears that the C-band scatterometer has higher correlation with sea state impacts to lead us to assume that Ku-band scatterometer seem to be much less impacted by changes in wave climate. We note that all scatterometer data discussed here is for incidence angles greater than 40 degree. We now compare the observed wind histogram shifts between altimeter- and scatterometer- retrieved wind speeds (last column of table 8). As above, we provide (in parenthesis) the computation made when restricting SWH to the range of  $2.5 \pm 0.5$  m/s.

The Ku-band altimeter appears to systematically overestimate wind speeds by about  $0.5 - 1.5$  m/s (in the high latitude area) when compared to Ku-band scatterometer estimates. There is essentially no shift between the altimeter and C-band ERS scatterometer estimates. Since such results are confirmed for fixed SWH values, this implies that SWH is not a perfect surrogate to describe the sea state. Physically, it can be postulated that, for a given SWH, the long waves are generally steeper in the Southern ocean than in the tropics where more gentle weak slope swell conditions dominate. Accordingly, altimeter backscatter levels will differ by region for identical wind speed and SWH - resulting in the observed systematic regional shift. One good regional example for this anticipated observation is given by Hwang et al. (1998). That study found that a site-specific altimeter wind speed algorithm for the Gulf of Mexico (closed basin) gave improved wind accuracy there in comparison to the open-ocean operational MCW routine. Their best algorithm made use of the significant slope parameter (not SWH) as derived from wave buoys.

Our preliminary conclusion regarding regional TOPEX wind biases is that a globally-applied altimeter wind speed algorithm will lead to systematic bias at levels of  $0.5-1.5$  m/s. The bias will be positive for the high latitudes and negative near the tropics. An altimeter GMF including SWH does not appear to remedy this problem.

## A Computing the Ku-band MLP solutions

### A.1 Ku-band $F_1$ algorithm

$$U = \frac{1}{1+e^{-(W_2 * X + B_2)}}$$

where

- $W_2 = \begin{pmatrix} 0.5401201 & 10.4048140 \end{pmatrix}, B_2 = -2.2838729$
- $X = \frac{1}{1+e^{-(W_1 * P + B_1)}}$

where

- $W_1 = \begin{pmatrix} -33.9506170 & -11.0339400 \\ -3.9342847 & -0.0583444 \end{pmatrix}, B_1 = \begin{pmatrix} 18.0637810 \\ -0.3722814 \end{pmatrix}$
- $P = \begin{pmatrix} m_{Ku} \times \sigma_{Ku}^o + b_{Ku} \\ m_{SwH} \times SwH + b_{SwH} \end{pmatrix}$

where

- $\sigma_{Ku}^o = \text{Ku-band radar backscatter (dB)}$
- $SwH = \text{significant wave height (meters)}$
- $m_{Ku} = 0.0690915, b_{Ku} = -0.3433598$
- $m_{SwH} = 0.0637450, b_{SwH} = 0.0872510$

To rescale U back into meters/sec :

$$Wind = \frac{U - b_{wind}}{m_{wind}}$$

where

$$m_{wind} = 0.0284394, b_{wind} = 0.1000000$$

## A.2 Ku-band $F_2$ algorithm

$$\sigma^o = \frac{1}{1+e^{-(W_2 * X + B_2)}}$$

where

- $W_2 = \begin{pmatrix} 1.1828134 & -3.3009623 \end{pmatrix}, B_2 = 1.1390633$
- $X = \frac{1}{1+e^{-(W_1 * P + B_1)}}$

where

- $W_1 = \begin{pmatrix} -43.3954100 & -6.9255032 \\ 2.7861243 & 1.2229266 \end{pmatrix}, B_1 = \begin{pmatrix} 7.8345911 \\ -1.4648877 \end{pmatrix}$
- $P = \begin{pmatrix} m_{wind} \times U_{10} + b_{wind} \\ m_{SwH} \times SwH + b_{SwH} \end{pmatrix}$

where

- $U_{10}$  = wind speed at 10 m height (m/s)
- $SwH$  = significant wave height (meters)
- $m_{wind} = 0.0284394, b_{wind} = 0.1000000$
- $m_{SwH} = 0.0637450, b_{SwH} = 0.0872510$

To rescale  $\sigma^o$  back into dB :

$$\sigma^o = \frac{\sigma^o - b_{Ku}}{m_{Ku}}$$

where

$$m_{Ku} = 0.0690915, b_{Ku} = -0.3433598$$

This should then be run on a high resolution ( $U_{10}, SwH$ ) grid and computation of the wind estimate is obtained through inversion of this grid.

## B Computing the C-band MLP solutions

### B.1 C-band $F_3$ algorithm

$$U = \frac{1}{1+e^{-(W_2 * X + B_2)}}$$

where

- $W_2 = \begin{pmatrix} 8.1711413 & 1.1434195 \end{pmatrix}, B_2 = -5.2023982$
- $X = \frac{1}{1+e^{-(W_1 * P + B_1)}}$

where

- $W_1 = \begin{pmatrix} -2.6574267 \\ 13.2138030 \end{pmatrix}, B_1 = \begin{pmatrix} 1.4835598 \\ -9.9643148 \end{pmatrix}$
- $P = (m_C \times \sigma_C^o + b_C)$

where

- $\sigma_C^o = \text{C-band radar backscatter (dB)}$
- $m_C = 0.1165226, b_C = -1.1973326$

To rescale U back into meters/sec :

$$Wind = \frac{U - b_{wind}}{m_{wind}}$$

where

$$m_{wind} = 0.0284394, b_{wind} = 0.1000000$$



## B.2 C-band $F_4$ algorithm

$$U = \frac{1}{1+e^{-(W_2 * X + B_2)}}$$

where

- $W_2 = \begin{pmatrix} -1.0820622 & 5.4657769 \end{pmatrix}, B_2 = -2.4234658$
- $X = \frac{1}{1+e^{-(W_1 * P + B_1)}}$

where

- $W_1 = \begin{pmatrix} -11.8509120 & 1.6738914 \\ -4.8002029 & -0.5681795 \end{pmatrix}, B_1 = \begin{pmatrix} 7.8895575 \\ 2.4730893 \end{pmatrix}$
- $P = \begin{pmatrix} m_C \times \sigma_C^\circ + b_C \\ m_{Sw h} \times Sw h + b_{Sw h} \end{pmatrix}$

where

- $\sigma_C^\circ = \text{C-band radar backscatter (dB)}$
- $Sw h = \text{significant wave height (meters)}$
- $m_C = 0.1165226, b_C = -1.1973326$
- $m_{Sw h} = 0.0642570, b_{Sw h} = 0.0807229$

To rescale U back into meters/sec :

$$Wind = \frac{U - b_{wind}}{m_{wind}}$$

where

$$m_{wind} = 0.0284394, b_{wind} = 0.1000000$$

### B.3 C-band $F_5$ algorithm

$$\sigma^o = \frac{1}{1+e^{-(W_2 * X + B_2)}}$$

where

- $W_2 = \begin{pmatrix} -1.5324596 & -11.4232230 \end{pmatrix}, B_2 = 7.8978416$
- $X = \frac{1}{1+e^{-(W_1 * P + B_1)}}$

where

- $W_1 = \begin{pmatrix} 29.3268750 & 8.3472182 \\ 0.8428848 & 0.4509337 \end{pmatrix}, B_1 = \begin{pmatrix} -6.3090396 \\ -0.1066253 \end{pmatrix}$
- $P = \begin{pmatrix} m_{wind} \times U_{10} + b_{wind} \\ m_{SwH} \times SwH + b_{SwH} \end{pmatrix}$

where

- $U_{10}$  = wind speed at 10 m height (m/s)
- $SwH$  = significant wave height (meters)
- $m_{wind} = 0.0284394, b_{wind} = 0.1000000$
- $m_{SwH} = 0.0642570, b_{SwH} = 0.0807229$

To rescale  $\sigma^o$  back into dB :

$$\sigma^o = \frac{\sigma^o - b_C}{m_C}$$

where

$$m_C = 0.1086088, b_C = -1.1092217$$

This should then be run on a high resolution ( $U_{10}, SwH$ ) grid and computation of the wind estimate is obtained through inversion of this grid.

## References

- [Benada 1997] BENADA R. – Merged gdr (topex/poseidon) generation b: user's handbook, 30 july, 1997. D-11007, JPL, PO-DAAC.
- [Bentamy et al. 1999] BENTAMY A., QUEFFEULOU P., QUILFEN Y. and KATSAROS K. – Ocean surface wind fields estimated from satellite active and passive microwave instruments. *IEEE Geoscience and Remote Sensing*, vol. 37, n° 5, 1999.
- [Brown et al. 1981] BROWN G.S., STANLEY H.R. and ROY N.A. – The wind speed measurement capability of spaceborne radar altimeters. *IEEE J. Oceanic Eng.*, vol. OE-6(2), 1981, pp. 59–63.
- [Callahan et al. 1994] CALLAHAN P.S., MORRIS C.S. and HSIAO S.V. – Comparison of Topex-Poseidon  $\sigma^o$  and significant wave height distributions to Geosat. *J. Geophys. Res.*, vol. 99, n° C12, 1994, pp. 25015–25024.
- [Cersat 1996] CERSAT. – Off-line wind scatterometer ers products, 1996. IFREMER, C2-MUT-W-01-IF.
- [Cersat 1997] CERSAT. – Collocated nscat/ers products, 1997. IFREMER, NSCAT-MUT-S-01-IF.
- [Chapron et al. 1995] CHAPRON B., KATSAROS K., ELFOUHAILY T. and VANDEMARK D. – A note on relationships between sea surface roughness and altimeter backscatter. *Air-Water Gas Transfer*. – AEON Verlag & Studio Hanau, Jähne B. and Monahan E.C. edition, 1995.
- [Chelton and McCabe 1985] CHELTON D.B. and MCCABE P.J. – A review of satellite altimeter measurement of surface wind speed: with a proposed new algorithm. *J. Geophys. Res.*, vol. 90, 1985, pp. 4707–4720.
- [Dobson et al. 1987] DOBSON E., MONALDO F., GOLDBIRSH J. and WILKERSON J. – Validation of Geosat altimeter derived wind speeds and significant wave heights using buoy data. *J. Geophys. Res.*, vol. 92, 1987, pp. 10719–10731.
- [Dunbar 1997] DUNBAR R. S. – Nasa scatterometer, high-resolution merged geophysical data product: User's guide, May, 1997. Ver 1.1, JPL, PO-DAAC.
- [Elfouhaily et al. 1997] ELFOUHAILY T., CHAPRON B., VANDEMARK D. and GOURRION J. – Estimation of wind stress using dual-frequency topex data. *J. Geophys. Res.*, vol. 103, n° C11, 1997, pp. 25,101–25,108.
- [Freilich and Challenor 1994] FREILICH M.H. and CHALLENGOR P.G. – A new approach for determining fully empirical altimeter wind speed model functions. *J. Geophys. Res.*, vol. 99, n° C12, 1994, pp. 25051–25062.
- [Freilich and Dunbar 1993] FREILICH M.H. and DUNBAR R.S. – Derivation of satellite wind model functions using operational surface wind analyses : an altimeter example. *J. Geophys. Res.*, vol. 98, 1993, pp. 14633–14649.

- [Freilich and Dunbar 1999] FREILICH M.H. and DUNBAR R.S. – The accuracy of the nscat-1 vector winds : comparison with ndbc buoys. *J. Geophys. Res.*, vol. 104, n° C5, 1999, pp. 11231–11246.
- [Glazman and Greysukh 1993] GLAZMAN R.E. and GREYSUKH A. – Satellite altimeter measurements of surface wind. *J. Geophys. Res.*, vol. 98, 1993, pp. 2475–2483.
- [Glazman and Pilorz 1990] GLAZMAN R.E. and PILORZ S. – Effects of sea maturity on satellite altimeter measurements of surface wind. *J. Geophys. Res.*, vol. 95, 1990, pp. 2857–2870.
- [Gower 1996] GOWER J.F.R. – Intercalibration of wave and wind data from Topex/Poseidon and moored buoys off the west coast of Canada. *J. Geophys. Res.*, vol. 101, n° C2, 1996, pp. 3817–3830.
- [Hagan et al. 1996] HAGAN M.T., DEMUTH H.B. and BEALE M. – Neural network design, 1996. 637 pp, PWS Publishing, MA.
- [Hwang et al. 1998] HWANG P.A., TEAGUE W.J., JACOBS G.A. and WANG D.W. – A statistical comparison of wind speed, wave height and wave period derived from satellite altimeters and ocean buoys in the Gulf of Mexico region. *J. Geophys. Res.*, vol. 103, n° C5, 1998, pp. 10451–10468.
- [Kohler 1988] KOHLER H. – Essentials of Statistics, 1988. 526 pp, Scott., Foresman and Company, Illinois.
- [Lefèvre et al. 1994] LEFÈVRE J.M., BARCKICKE J. and MÉNARD Y. – A significant wave height dependent function for topex/poseidon wind speed retrieval. *J. Geophys. Res.*, vol. 99, n° C12, 1994, pp. 25035–25046.
- [Monaldo and Dobson 1989] MONALDO F. and DOBSON E. – On using significant wave height and radar cross section to improve radar altimeter measurements. *J. Geophys. Res.*, vol. 94, n° C9, 1989, pp. 12699–12701.
- [Queffeulou et al. 1999] QUEFFEULOU P., CHAPRON B. and BENTAMY A. – Comparing ku band nscat scatterometer and ERS-2 altimeter winds. *IEEE trans. geoscience and remote sensing.*, vol. 37, 1999, pp. 1662–1670.
- [Sterling and Pollack 1996] STERLING T.D. and POLLACK S.V. – Introduction to statistical processing, 1996. 663 pp., Prentice-Hall, New Jersey.
- [Tournadre and Blanquet 1994] TOURNADRE J. and BLANQUET S. – Wind and wave mesoscale variability from in situ and altimeter data. *Global Atmosphere and Ocean System*, vol. 2, 1994, pp. 221–247.
- [Wentz and Smith 1999] WENTZ F.J. and SMITH D.K. – A model function for the ocean normalized radar cross section at 14 GHz derived from nscat. *J. Geophys. Res.*, vol. 104, n° C5, 1999, pp. 11499–11514.

- [Witter and Chelton 1991] WITTER D.L. and CHELTON D.B. – A geosat altimeter wind speed algorithm and a method for altimeter wind speed algorithm development. *J. Geophys. Res.*, vol. 96, n° C5, 1991, pp. 8853–8860.
- [Wu 1999] WU J. – On wave dependency of altimeter sea returns - weak fetch influence on short ocean waves. *J. Atmos. Ocean. Tech.*, vol. 16, 1999, pp. 373–378.
- [Young 1993] YOUNG I.R. – An estimate of the Geosat altimeter wind speed algorithm at high wind speeds. *J. Geophys. Res.*, vol. 93, n° C11, 1993, pp. 20275–20286.